Matter

CellPress

Article

On the intrinsic reaction kinetics of polypropylene pyrolysis

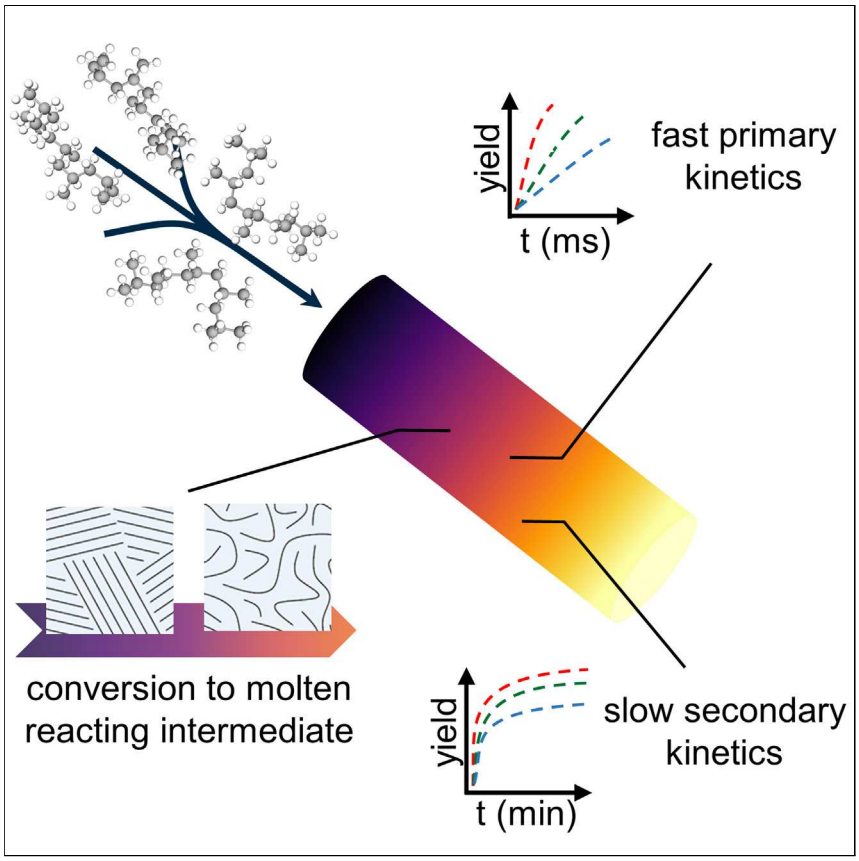

The global plastic waste challenge necessitates the development of technologies, such as pyrolysis, that will enable a circular plastic economy. In this work, we establish a method of pyrolyzing polypropylene absent heat and mass transfer limitations and quantify the intrinsic reaction kinetics of polypropylene pyrolysis. We describe the reaction kinetics via a lumped first-order consumption model with a comparison to first-principles calculations and literature models. Additionally, we establish the presence of multiple kinetic regimes during polypropylene pyrolysis.

Nathan Sidhu, Isaac Mastalski, Ali Zolghadr, ..., Ziwei Wang, Matthew Neurock, Paul J. Dauenhauer

hauer@umn.edu

Highlights

PHASR pyrolyzes polypropylene absent transport limitations

The intrinsic kinetics of polypropylene are quantified for the first time

Polypropylene pyrolysis may be described by a two-stage lumped reaction system

3 **Understanding**
Dependency and conditional studies on material behavior

Sidhu et al., Matter 6, 3413–3433
October 4, 2023
https://doi.org/10.1016/j.matt.2023.07.020

Matter

CellPress

Article

On the intrinsic reaction kinetics of polypropylene pyrolysis

Nathan Sidhu,[1,2] Isaac Mastalski,[1,2] Ali Zolghadr,[1] Bryan Patel,[3] Sundararajan Uppili,[3] Tony Go,[3] Saurabh Maduskar,[3] Ziwei Wang,[1] Matthew Neurock,[1] and Paul J. Dauenhauer[1,2,4,*]

SUMMARY

The growing global plastic waste challenge requires development of new plastic waste management strategies, such as pyrolysis, that will help to enable a circular plastic economy. Developing optimized, scalable pyrolysis reactors capable of maximizing the yield of desired products requires a fundamental understanding of plastic pyrolysis chemistry. Accordingly, the intrinsic reaction kinetics of polypropylene pyrolysis have been evaluated by the method of pulse-heated analysis of solid reactions (PHASR), which enables time-resolved measurement of pyrolysis kinetics at high temperature absent heat and mass transfer limitations on the millisecond scale. Polypropylene pyrolysis product evolution curves were generated at 525°C–625°C, and the overall reaction kinetics were described by a lumped first-order model with an activation energy of 242.0 ± 2.9 kJ mol^{-1} and a pre-exponential factor of 35.5 ± 0.6 ln(s^{-1}). Additionally, the production of solid residues formed during polypropylene pyrolysis was investigated, revealing a secondary kinetic regime.

INTRODUCTION

Plastics are ubiquitous materials because of their unique combination of useful material properties and affordability. Since the 1950s, industrial-scale production of plastics has grown from an estimated two million metric tons (Mt) annually to approximately 438 Mt as of 2017.[1] Based on current trends, the annual rate of plastic production is projected to exceed one billion tons by 2050.[1] This massive growth in plastic production has resulted in the generation of an immense amount of plastic waste, particularly because of the large fraction of plastics being produced for single-use applications, such as packaging.[2] As of 2017, approximately 7,000 Mt of plastic waste have been generated, and it is projected that this cumulative quantity will grow to 33,000 Mt by 2050.[1] Effective waste management strategies must be developed to manage existing and future plastic waste. Polypropylene (PP) is particularly important to the plastic waste problem; PP is the most widely produced thermoplastic material, accounting for around 17% of annual global plastic production, 18% of plastic packaging, and 24% of plastic in municipal solid waste.[1,3–5]

End-of-life (EOL) plastics that have exceeded their useful product life are conventionally considered waste products. EOL plastics are primarily discarded in landfills, accumulating as plastic waste.[1,6] As of 2017, 76% of all plastic waste generated globally was discarded, 14% was incinerated, and only 10% was recycled.[1] While incineration allows for energy recovery and prevents plastic waste accumulation, it still leads to the release of CO_2 and other environmental toxins (e.g., dioxins) and prevents reuse of the plastics.[6–8]

PROGRESS AND POTENTIAL

The rapid and continual growth of the global plastic market and the associated global plastic waste challenge necessitate the development of new approaches to plastic waste management, such as pyrolysis, that will enable a circular plastic economy. Previous attempts to measure the reaction kinetics of plastic pyrolysis, which are essential for developing a fundamental understanding of plastic pyrolysis and designing optimized pyrolysis reactors, have been unable to decouple chemistry from transport artifacts and individual experimental conditions. Here, we demonstrate that the method of pulse-heated analysis of solid reactions (PHASR) is capable of pyrolyzing polypropylene absent transport limitations and quantifying the intrinsic reaction kinetics of polypropylene pyrolysis on the millisecond timescale. Additionally, we identify the presence of multiple kinetic regimes, providing chemical kinetics for all future polypropylene pyrolysis studies.

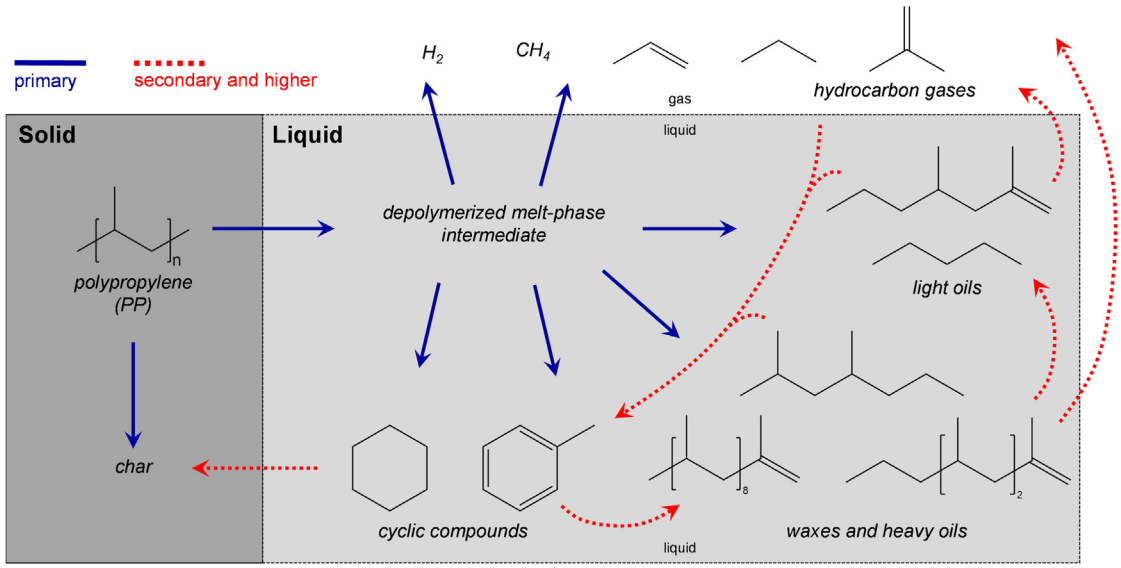

Figure 1. PP pyrolysis network

PP undergoes primary (solid blue pathways) thermal conversion via radical reactions to produce solid, liquid, and gaseous products, which may undergo secondary and higher-order reactions (red dashed pathways).

Recycling offers a route through which plastics can be reused, but traditional mechanical recycling is incapable of converting plastics back to their original form in most cases. The methods involved in thermomechanical processing (e.g., remelting and pelletizing) result in degradation of the plastic material, requiring addition of virgin plastics to improve material properties; alternatively, these mechanically recycled plastics can be downcycled and eventually discarded.[6,8,9] Mechanical recycling is also sensitive to mixed waste streams and impurities, leading to reductions in material quality and increased costs.[6–10] Continued use of these traditional waste management strategies fails to address the global plastic waste problem.

Chemical recycling is an alternative approach to plastic waste management that can help to enable a circular economy in which EOL plastics are utilized as a resource to produce new plastics and chemicals.[6–9,11] Many chemical recycling processing options exist, including solvolysis, hydrolysis, and pyrolysis.[8,9,12–14] Pyrolysis is the thermal conversion of a material in an inert oxygen-free environment to produce a variety of liquids and gases, including plastic monomers; this processing method can accommodate highly heterogeneous and contaminated plastic waste streams, making it more cost effective at scale.[3,9,10,15]

The chemistry of PP pyrolysis is highly complex, involving many intermediates and products. A detailed description of the reaction network and associated reaction kinetics that matches experimental data does not yet exist, with current models providing incomplete descriptions using empirical formulas or sets of elementary steps.[16–20] Figure 1 illustrates several of the many reaction pathways and product groups that have been reported for PP pyrolysis.[16,19–69] While there is not yet a complete understanding of PP pyrolysis, there is a generally accepted reaction scheme. First, PP melts and depolymerizes via random chain scission, producing radical intermediates. The radical intermediates react to form primary products, represented by the solid blue pathways. The primary products can then undergo further reactions (e.g., interconversion and Diels-Alder), represented by the dashed red pathways, forming secondary and higher products.[19,20,24,70]

[1]Department of Chemical Engineering & Materials Science, University of Minnesota, 421 Washington Ave. SE, Minneapolis, MN 55455, USA

[2]Center for Sustainable Polymers, University of Minnesota, Minneapolis, MN 55455, USA

[3]ExxonMobil Technology and Engineering Company, 5200 Bayway Dr., Baytown, TX 77520, USA

[4]Lead contact

*Correspondence: hauer@umn.edu

https://doi.org/10.1016/j.matt.2023.07.020

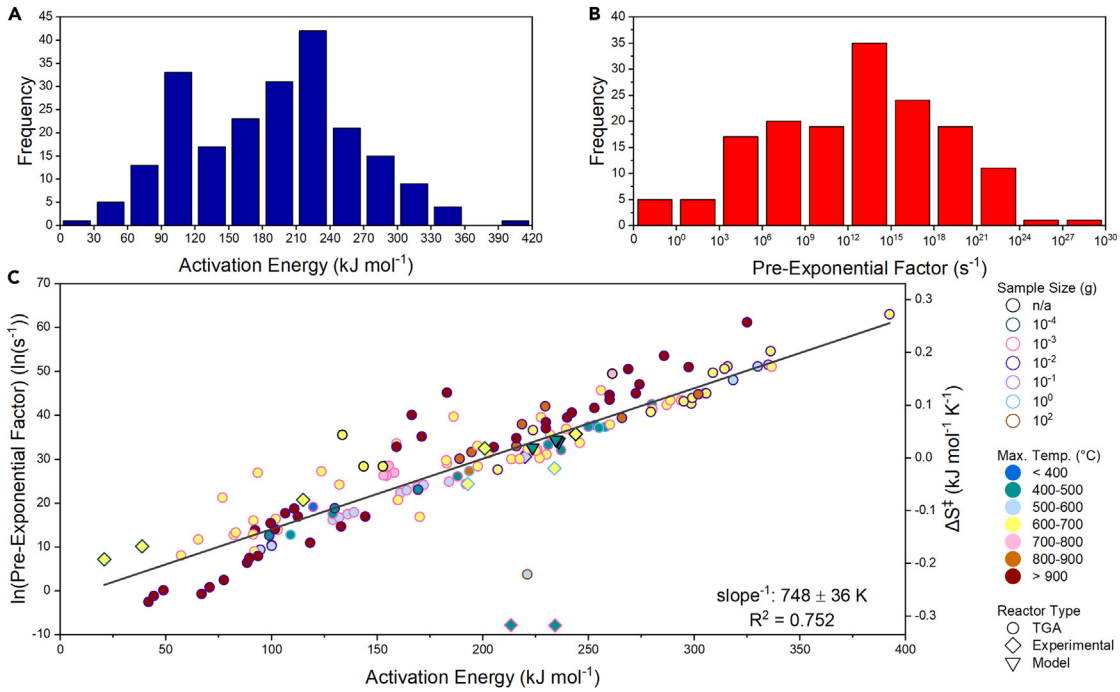

Figure 2. Literature-reported lumped PP pyrolysis kinetics

(A) Distribution of reported activation energies.

(B) Distribution of reported pre-exponential factors.

(C) Compensation plot of pre-exponential factor (left axis) and activation entropy (right axis) versus activation energy, with associated experimental parameters provided for each data point.

While there is some agreement on the general structure of the PP pyrolysis reaction network, there is little agreement on the underlying kinetics of the process, with significant variation in reported product distributions and reaction kinetic parameters. For example, reported lumped activation energies vary between 21 and 393 kJ mol^{-1}, and reported pre-exponential factors differ by up to 27 orders of magnitude.[48,55,63] The variation in the available data is further demonstrated by Figure 2, which presents 215 reported apparent activation energies and pre-exponential factors for PP pyrolysis from 50 literature sources; complete details on the data presented in this figure are available in the supplemental information. These discrepancies can be attributed to variations in experimental conditions, such as heating and cooling rates, residence time, and reactor design.[23,55,71–76] Additionally, heat and mass transfer limitations are often present because of large sample length scales (e.g., pellets and packed powders), which produce a distribution of reaction kinetics in the pyrolyzing mass.[18,71,74,75,77–81] The influence of operational conditions on the kinetic parameters indicates that previous studies have reported apparent kinetics with transport artifacts rather than intrinsic reaction kinetics.

Intrinsic reaction kinetics will be essential for developing a fundamental understanding of PP pyrolysis and for the design and optimization of scalable pyrolysis reactors.[82] To study the intrinsic reaction kinetics of PP pyrolysis, a reactor system absent heat and mass transport limitations is required that also can measure the time-resolved evolution of the polymer and its pyrolysis products. To this end, the pulse-heated analysis of solid reactions (PHASR) reactor was redesigned for polyolefin pyrolysis and validated with low-density polyethylene.[83] In this work, use of the PHASR reactor with PP was validated, and isothermal, reaction-controlled

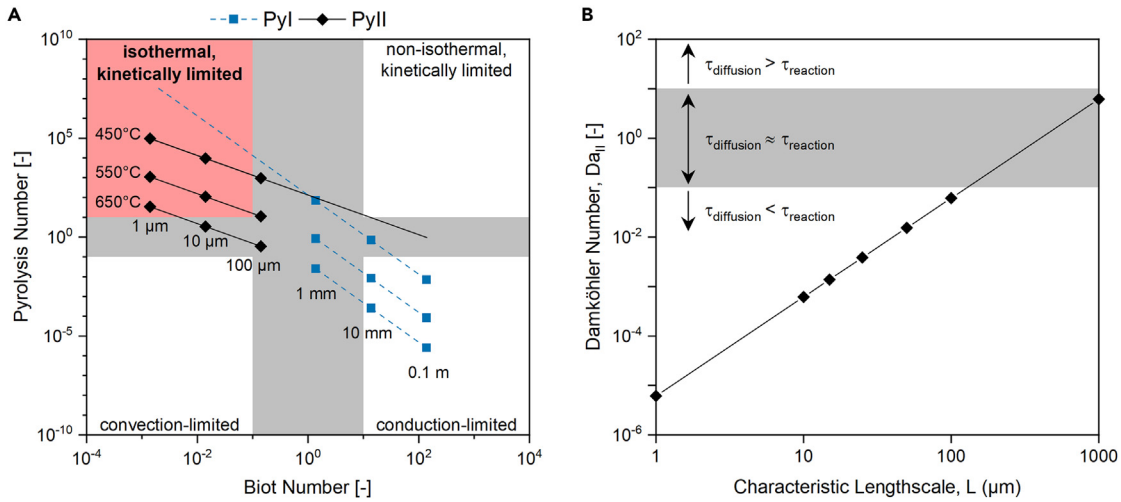

Figure 3. PP transport properties

(A) Pyrolysis map comparing the two pyrolysis numbers and the Biot number, providing an order-of-magnitude estimation for the length scales and temperatures at which reaction-controlled pyrolysis is possible.

(B) Mass transport map comparing the second Damköhler number with the characteristic length scale (i.e., thickness) of a PP sample, providing an order-of-magnitude estimate for the length scale leading to the onset of transport limitations. Further information on these analyses is provided in the supplemental information.

operation was demonstrated, yielding PP pyrolysis evolution curves between 525°C and 625°C that are then compared with literature data. Lastly, the solid residues formed during PP pyrolysis were analyzed to understand the competing pathways to volatile and non-volatile PP products.

RESULTS AND DISCUSSION

Verification of isothermal, reaction-controlled operation

To obtain intrinsic reaction kinetics, it was necessary to operate under reaction-controlled conditions. To determine the limiting parameters (reaction temperature and sample length scale) of the regime in which PP pyrolysis occurs absent transport limitations, dimensional analyses of the heat and mass transfer properties of the reacting PP system were performed. To analyze the heat transport characteristics of the PP system, the pyrolysis numbers (Py^{I} and Py^{II}) were plotted against the Biot number (Bi), producing a pyrolysis map (Figure 3A). Py^{I} and Py^{II} relate the timescale of reaction to the timescales of conduction and convection, respectively, and the timescales of conduction and convection are compared by Bi (Equations S3.1–S3.3). The resulting order-of-magnitude estimate of this analysis indicates that it is possible to measure the intrinsic reaction kinetics of PP pyrolysis at temperatures up to ~650°C with sample length scales of order 10 μm or less, as described by the top left section highlighted in Figure 3A, where heat transport (conduction and convection) occurs faster than reaction. An analogous dimensional analysis was performed for mass transfer within a PP sample. Here, the second Damköhler number (Da_{II}), the ratio of the rate of reaction to the rate of mass diffusion, was plotted against the characteristic length scale of PP (i.e., the sample thickness), as shown in Figure 3B. This analysis shows that PP samples with length scales of order 100 μm or thinner are reaction controlled, with diffusion occurring orders of magnitude faster than reaction. Definitions, selected parameters, assumptions, and associated calculations for all dimensional quantities are provided in Equations S3.1–S3.4 and Tables S3.1 and S3.2.

The dimensional analyses indicate that heat transfer limitations are more likely to arise than mass transfer limitations, demonstrated by the difference in the

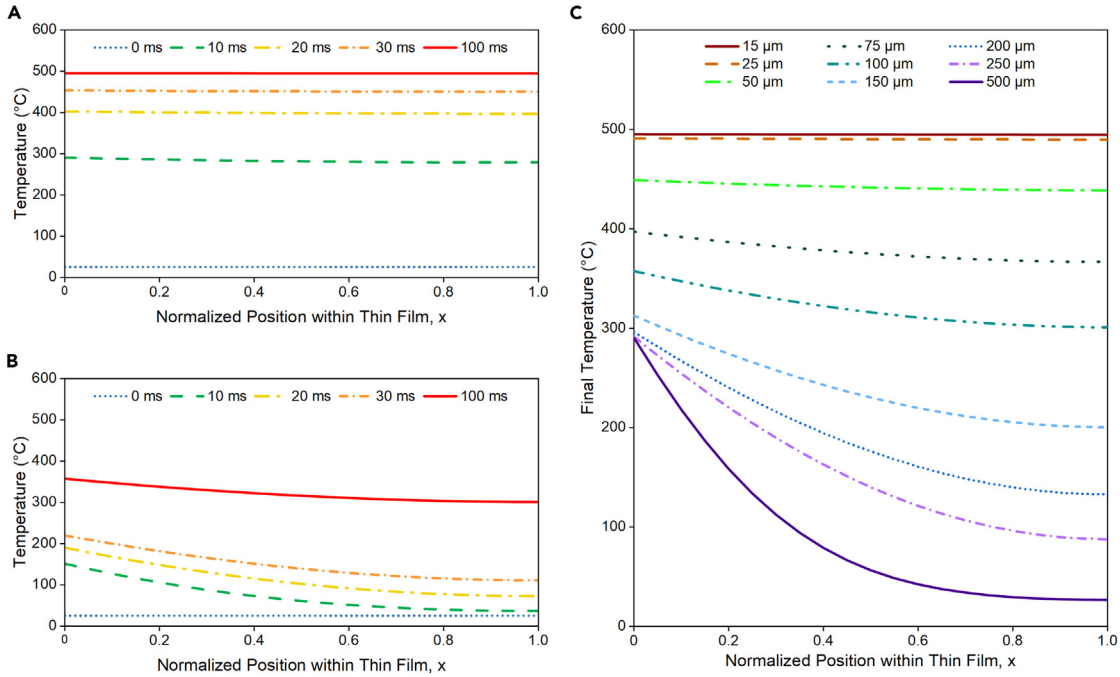

Figure 4. Simulated transient temperature profiles in PP films

(A) 15-µm-thick sample with a target temperature of 500°C

(B) 100-µm-thick sample with a target temperature of 500°C

(C) Final temperatures for samples of different thicknesses after 100 ms of heating and a target temperature of 500°C.

order-of-magnitude estimates for the maximum allowable sample length scale to maintain reaction-controlled conditions (10 µm vs. 100 µm). Heat transport was further analyzed with a 1D simulation in MATLAB. The simulated system, a PP film atop a steel sample plate with a He atmosphere, includes conduction at the film/plate interface, conduction through the film, reaction kinetics throughout the film, and convection at the film/atmosphere interface. All selected parameters and complete simulation details are provided in Equations S3.5–S3.8 and Table S3.3. Figures 4A and 4B show the same transient temperature profiles for simulated PP films with thicknesses of 15 µm and 100 µm, respectively, being heated to a target reaction temperature of 500°C. The 15-µm film heated rapidly and uniformly, reaching ~300°C in the first 10 ms and approximately reaching the 500°C set point after just 30 ms of heating. Conversely, the 100-µm film was shown to heat in a non-ideal fashion, with large temperature gradients observed at all times; the maximum film temperature was more than 100°C below the target temperature after 100 ms of heating. The effect of sample thickness on heat transport is further demonstrated by Figure 4C, which plots the simulated temperature profiles of films with thicknesses ranging between 15 µm and 500 µm after 100 ms of heating. These data show that even a small increase in film thickness from 15 µm to 25 µm results in a lower film temperature at 100 ms; however, the profile is still highly uniform. At all greater thicknesses, there is a notable decrease in film temperature and increasing non-uniformity in the thermal profiles. The results of these simulations further demonstrate the necessity for fine control over the length scales of the PP samples to achieve isothermal, reaction-controlled pyrolysis conditions.

The dimensional analyses and heat transport simulations rely on parameters found in the literature that are non-specific to the material and reactor used for this work and therefore can only provide an order-of-magnitude estimate for the maximum film

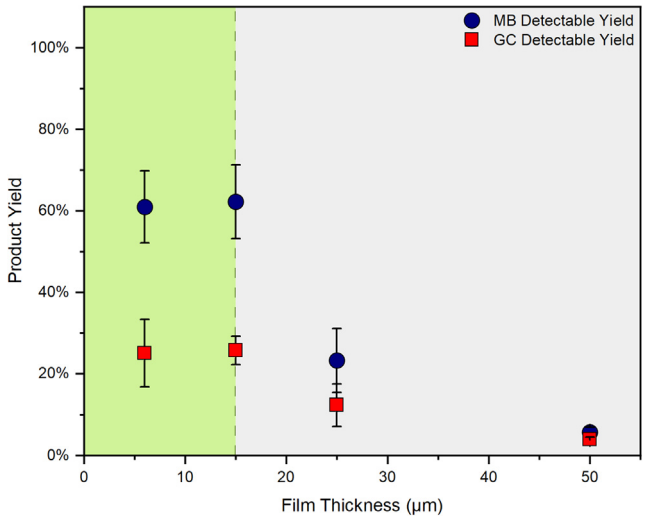

Figure 5. Experimental verification of the transition between reaction-controlled and transport-controlled operation

Product yields detected by gas chromatography (GC; red squares) and microgram-resolution balance (MB; navy circles) are plotted as a function of sample film thickness for pyrolysis reactions performed at 625°C for 60 ms. Pyrolysis reactions performed with samples thinner than 15 μm are reaction controlled (green region) and transport controlled (gray region) when performed with samples thicker than 15 μm. The error bars represent the standard deviation of the data points.

thickness and reaction temperatures that define the isothermal, reaction-controlled regime. Given this limitation, the transition between the transport-controlled and reaction-controlled PP pyrolysis regimes was experimentally verified. Here, a series of PP films of thicknesses ranging between 6 μm and 50 μm were prepared and pyrolyzed in the PHASR reactor at 625°C for 60 ms. A minimum of three reactions were performed for each thickness, and the product yields, measured by gas chromatography (GC) and microgram-resolution balance (MB), are plotted in Figure 5. For the 15-, 25-, and 50-μm-thick samples, a continuous decrease in GC- and MB-detectable yields was observed with increasing thickness, demonstrating that the experiments are transport limited at thicknesses greater than 15 μm, with the limitations increasing as a function of thickness. In contrast, the observed product yields were equal for PP samples with thicknesses of 6 and 15 μm, indicating reaction-controlled conditions absent heat and mass transfer limitations at thicknesses less than or equal to 15 μm. Through the combined theoretical and experimental results, it is clear that PP pyrolysis via the PHASR method results in isothermal, reaction-controlled conditions capable of quantifying intrinsic reaction kinetics.

Visual PHASR

Pyrolysis of PP films was observed with high-speed photography (1,000 fps) at 500°C, 550°C, 600°C, 650°C, and 700°C for 2 s within the visual PHASR reactor. The PHASR reactor and visual PHASR reactor are limited to reaction times of 2.0 s under standard operation because of an inherent safety limit of the PHASR power supply controller. Additional details are provided in the Secondary PP pyrolysis kinetics section. In all experimental trials, 15-μm thick, 3-mm-diameter PP samples were used. Individual frames from the high-speed video (at 0, 0.4, 0.8, 1.2, 1.6, and 2.0 s) are shown in Figures 6 and 7, and the original videos are available in real time and slow motion in Section S6. In all cases, the PP thin films are observed to react in a uniform manner, further establishing that the PHASR method enables isothermal, reaction-controlled conditions. Additionally, these videos enable a qualitative assessment of the rate and extent of reaction.

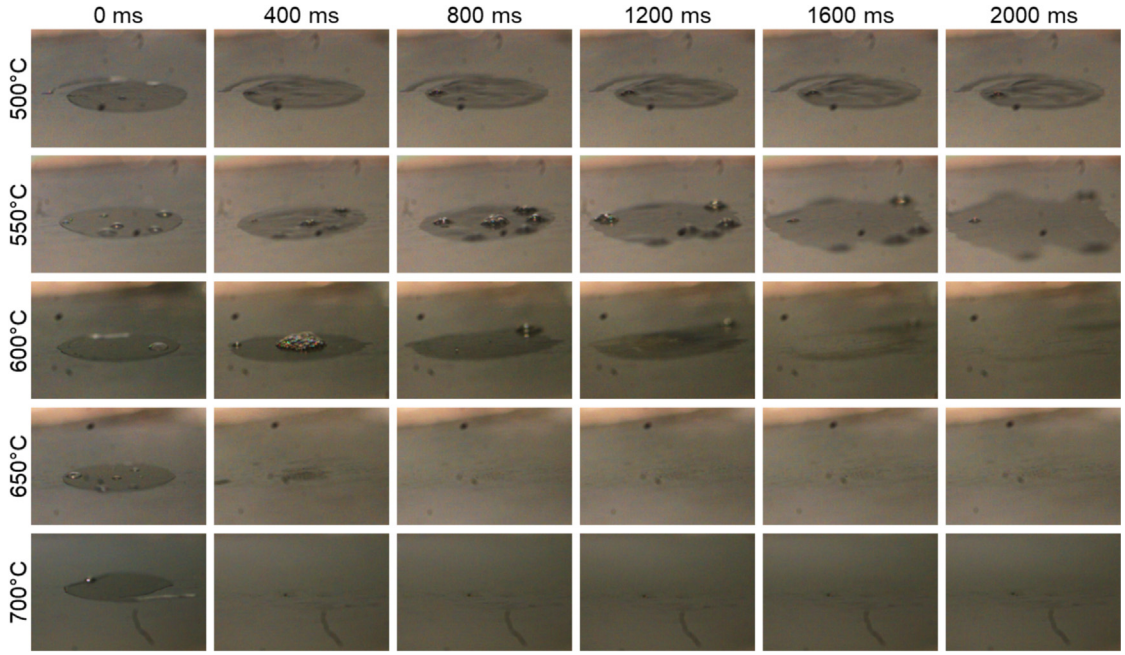

Figure 6. Visual PHASR: Side view
Shown are individual frames of high-speed video (1,000 fps) of PP thin films pyrolyzed at 500°C–700°C for 2.0 s in the visual PHASR reactor.

At 500°C, the apparent extent and rate of reaction are low, with little visual change to the sample occurring and large amounts of residue remaining on the plate after 2 s. At 550°C and 600°C, notable changes occurred to the samples as the reactions proceeded at a greater rate with less residue remaining after 2 s. At the highest reaction temperatures of 650°C and 700°C, the reactions occurred rapidly, reaching completion in less than 0.5 s, with the solid films rapidly forming a molten phase and eventually transforming into fully evolved vapors and gases with no observable residue remaining on the plates.

High-speed photography of reacting PP films also revealed complex multi-phase behavior, including the formation of bubbles, the generation of aerosols, and a potential Leidenfrost effect of the PP droplet on the hot plate, as shown in additional frames of the video of a PP film reacting at 600°C in Figure 8. At all temperatures, bubbles were observed to form with the evolution of volatile species in the melt phase, with the degree of bubble formation greatly increasing as a function of temperature. At 500°C and 550°C, small pockets of bubbles formed that remained independent, while bubbles formed throughout the reacting films and rapidly coalesced as the reaction proceeded at temperatures greater than or equal to 600°C. The presence of bubbles agrees with prior descriptions and observations of PP pyrolysis in the literature.[84,85] It is known that the presence and subsequent bursting of bubbles may lead to aerosol generation.[86] The majority of aerosols formed, either by bubble film fragmentation or jet ejections, likely existed at a size below the observable limit afforded by video resolution; however, jet ejection of a large aerosol (>2 μm) was observed at 600°C. This jet ejection event is shown in Figure 8 in the frames for reaction times spanning 428–432 ms. At 550°C and 600°C, the bubbles that formed moved along the surface of the sample plate. As shown in Figure 6, the small pockets of bubbles formed at 550°C spread from the center of the sample plate in multiple directions. At 600°C, as shown in Figures 6 and 8, a primary cluster of bubbles formed that moved toward the back right side of the plate. At 650°C and 700°C,

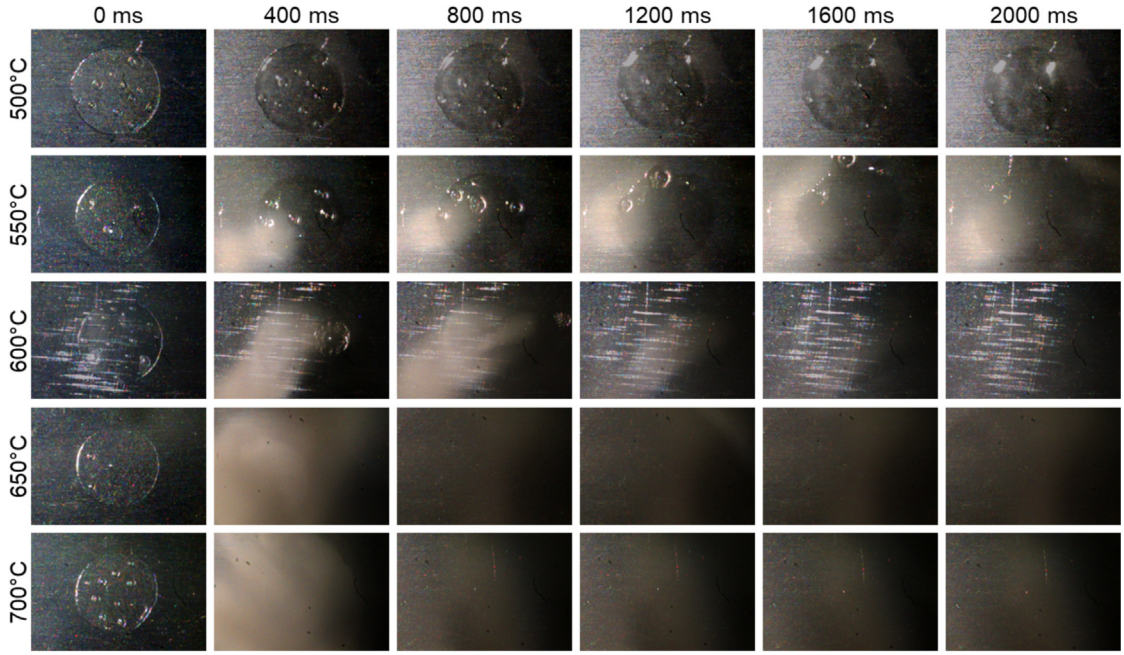

Figure 7. Visual PHASR: Top view
Shown are individual frames of high-speed video (1,000 fps) of PP thin films pyrolyzed at 500°C–700°C for 2.0 s in the visual PHASR reactor.

significant sample movement was not observed, which may be due to the high rate of reaction at these temperatures. The sample movement may be evidence of a Leidenfrost effect; however, the movement may have also been induced by the helium atmosphere sweeping through the visual PHASR reactor.

Intrinsic PP reaction kinetics

To measure the intrinsic reaction kinetics of PP pyrolysis, PP pyrolysis reactions were performed via the PHASR method at 525°C, 550°C, 575°C, 600°C, and 625°C for reaction times ranging between 20 ms and 2.0 s. A minimum of three reaction trials were conducted for each unique time and temperature condition, and all yield data from these reactions are shown in Figure 9. Volatile products up to C_{20} were quantified as the GC-detectable product yield (Figure 9A), and the total yield of volatile products by mass was quantified as the MB-detectable product yield (Figure 9B). Detailed definitions of the GC-detectable and MB-detectable yields are provided under Experimental procedures. In the GC- and MB-detectable product yields, it was observed that a maximum was reached at all temperatures between 140 ms (625°C) to 300 ms (525°C). Further increases in product yields were not observed in the additional reaction period up to 2.0 s. Furthermore, the measured product yields agreed well with the qualitatively observed extent of reaction in the visual PHASR reactor. In the visual PHASR experiments at 500°C and 550°C, large amounts of residue were observed to remain on the plate, while at 600°C or greater, little to no residue remained after 2.0 s of reaction. The maximum MB-detectable product yields increased from ~15% at 525°C to ~95% at 625°C. Even in cases where no visible residue remained, typical of reactions at 625°C for reactions times greater than 140 ms, the 1,2,4-trichlorobenzene cleaning process revealed that a small amount of residue was still present (~1 μg).

To describe the kinetics of the primary reaction mechanism of PP pyrolysis outlined in Figure 1, a first-order consumption model (Equation 1) was fit to the experimental

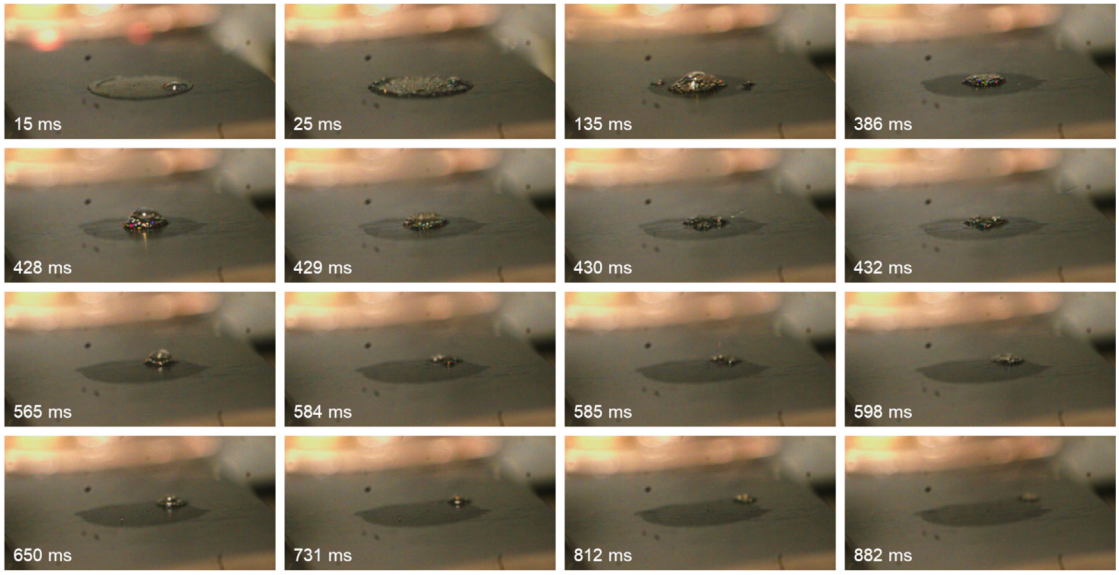

Figure 8. Visual PHASR: Observed reaction phenomena

Shown are individual frames of high-speed video (1,000 fps) of a PP thin film pyrolyzed at 600°C for 2.0 s in the visual PHASR reactor, depicting bubble formation, sample movement because of a potential Leidenfrost effect, and aerosol ejection.

data. As demonstrated in the Verification of isothermal, reaction-controlled operation section, the PHASR reactor operates under isothermal, reaction-controlled conditions. Accordingly, the first-order model purely describes the fundamental chemistry of the process, free of transport artifacts. The kinetic parameters were fit using the short reaction time data, which encompasses the observed initial period of reactivity. In Figures 10A and 10B, the model fits are plotted as solid lines, and the 95% confidence intervals are plotted as dashed lines, overlaying the short reaction time yield data up to 300 ms. In Figure 10C, the Arrhenius plot is provided for both models, and the values of the kinetic parameters are listed in Table 1. Further details are provided in Tables S4.1, S4.2, and S4.5; Figure S4.1; and Equations S4.29 and S4.30. Given that the MB-detectable product yields represent all products that volatilize at a given reaction temperature, the MB-detectable model parameters better describe the overall intrinsic reaction kinetics of PP pyrolysis, while the GC-detectable model parameters describe the intrinsic kinetics for the production of light species up to C_{20}.

$$Y(t) = 1 - e^{-kt} \qquad \text{(Equation 1)}$$

Comparison of measured intrinsic reaction kinetics with literature data

As shown in Figure 2, a vast range exists in the literature for the reported kinetics of PP pyrolysis, attributed to the measurement of apparent kinetics unique to a given experimental system rather than the intrinsic kinetics of the chemistry itself. The data presented in Figures 2A (reported apparent activation energies) and 2B (reported pre-exponential factors) were plotted together in Figure 2C as a compensation plot. In addition, the pre-exponential factors were converted to activation entropy ($\Delta S^{\ddagger}$; Figure 2C, right axis) using Equation 2. In Equation 2, e is the natural logarithm base, k_b is the Boltzmann constant, h is the Planck constant, T is the absolute temperature, and R is the universal gas constant.[87] The line of best fit for $\Delta S^{\ddagger}$ versus E_a (black line) provides the compensation slope, which was found to be 748 $\pm$ 36 K. Figure 2C also contains additional information on the sample sizes (symbol outlines), maximum reaction temperatures (symbol fill colors), and reactor types (symbol shapes) associated with the kinetic data. The

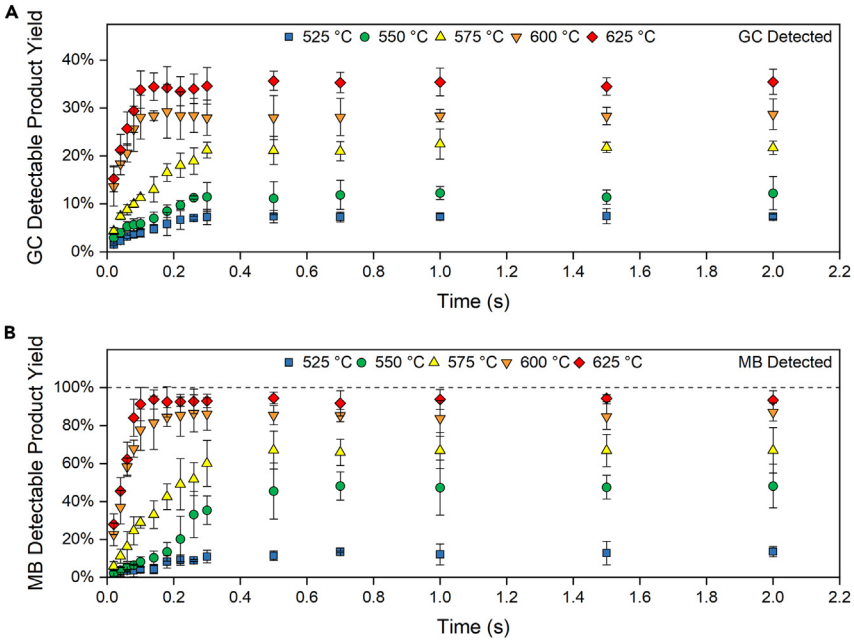

Figure 9. PP pyrolysis yield versus time

(A) Yield of light products (<C20) measured by GC.

(B) Yield of all volatile products measured by MB.

The error bars represent the standard deviation of the data points.

literature data in this analysis are tabulated in the supplemental information. The linear relationship between ln k_0 and E_a observed in the compensation plot is an apparent compensation effect[88,89] that further indicates that the literature-reported kinetics of PP pyrolysis are representative of apparent rather than intrinsic kinetics. The kinetic parameters measured in this work (Table 1), are intrinsic to PP pyrolysis and are within the range of the previously reported parameters, aligning with the centers of the distributions conveyed in Figure 2, particularly the overall intrinsic kinetic parameters represented by the MB-detected model.

$$k_0 = \frac{e k_b T}{h} e^{\frac{\Delta S^{\ddagger}}{R}} \qquad \text{(Equation 2)}$$

A mechanistic kinetic model to describe PP pyrolysis and calculate estimates for the apparent activation energy was also derived. The radical reaction model was based on the Rice-Herzfeld mechanism, commonly used to describe hydrocarbon chain decomposition and polyolefin pyrolysis (Reactions SR4.1–SR6).[56,90–95] The model simply describes PP pyrolysis as a general radical reaction system in terms of initiation, propagation, and termination. Full details of the model derivation are provided in Equations S4.2–S4.24, and the derived rate expression is described by Equation 3. Here, k_i, k_H, k_β, and k_t are the rate constants for initiation, propagation (via hydrogen abstraction and β-scission), and termination, respectively. Species *A* represents the reacting PP.

$$r_A = \frac{d[A]}{dt} = k_H \left(\frac{k_i}{k_t}\right)^{1/2} \left(\frac{[A]^{3/2}}{1+\frac{k_H}{k_\beta}[A]}\right) \qquad \text{(Equation 3)}$$

Values were calculated for the elementary steps of the Rice-Herzfeld mechanism via DFT following a previously described method and utilized in combination with the derived rate expression to calculate apparent activation energies for PP pyrolysis.[96]

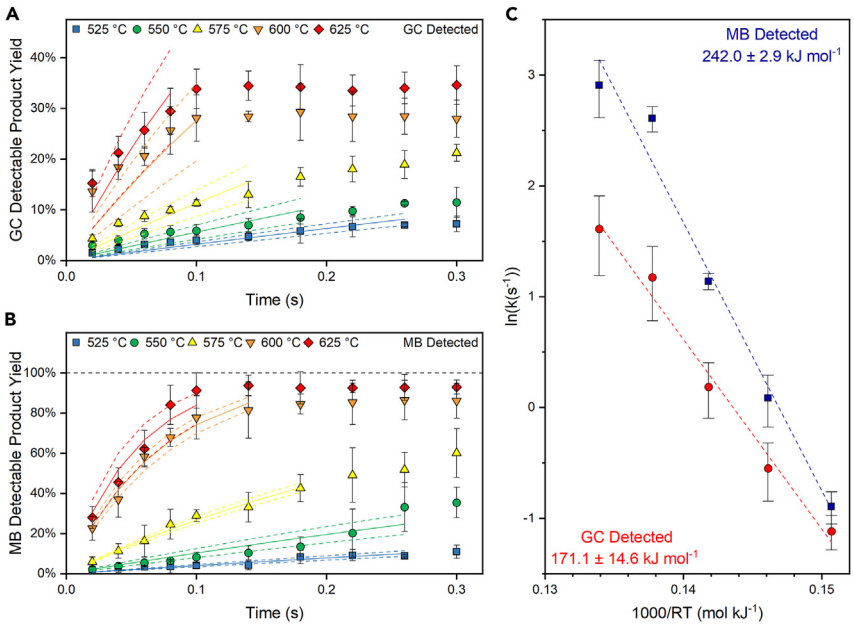

Figure 10. Kinetic analysis of PP pyrolysis yield versus time

(A) Yield of light products ($<C_{20}$) measured by GC (points) with first-order model fits (solid lines).

(B) Yield of all volatile products measured by MB (points) with first-order model fits (solid lines).

(C) Arrhenius plot of GC-detected (red circles) and MB-detected (navy squares) model fits, with linear regression analysis for determination of kinetic parameters. Complete details of model fitting are provided in the supplemental information.

The error bars represent the standard deviation of the data points.

Details on the DFT calculation methods are provided in the supplemental information. The DFT values were calculated for initiation via alkane C-C bond cleavage (~358 kJ mol^{-1}), propagation via β-scission (~117 kJ mol^{-1}), and propagation via hydrogen abstraction (~41 kJ mol^{-1}), and termination via radical recombination was assumed to have no energetic cost.[96] Three different termination mechanisms are considered for this model (R_1R_1, R_2R_2, and R_1R_2), and the apparent activation energy of the system depends on which of these mechanisms is dominant. The DFT activation energies were used to calculate the activation energies for R_1R_1-, R_2R_2-, and R_1R_2-dominant termination, resulting in activation energies of 220, 296, and 258 kJ mol^{-1}, respectively (Equations S4.25–S4.28). The calculated values are consistent with the intrinsic kinetic model parameters obtained experimentally via the PHASR method (Table 2) and with the range of literature-reported parameters (Tables S1.1A–S1.1R). Additional details on use of the DFT-calculated values with the derived rate expression are provided in Tables S4.3 and S4.4.

Residue analysis

Formation of residue product was observed at all reaction conditions other than 625°C for reaction times exceeding 100 ms. Residue and char from PP pyrolysis has been reported previously; however, there is little consistency in the definitions of the solids and varying extent of formation.[49,70,97–108] Given the consistent nature of residue formation in our experiments of Figure 9, the resulting solid residues from PP pyrolysis were characterized. Solid residues were analyzed by multiple methods, including microscopy, ^{13}C solid-state NMR, Raman spectroscopy, and attenuated total reflectance infrared (ATR-IR) spectroscopy. Other techniques, such as gel permeation chromatography (GPC), were not utilized because of low residue

Table 1. Intrinsic kinetic model parameters

	E_a (kJ mol^{-1})	$\ln(k_0)$ ($\ln[s^{-1}]$)
GC-detected	175.1 ± 13.1	25.2 ± 2.2
MB-detected	242.0 ± 2.9	35.5 ± 0.6

masses. The PP thin films used in the PHASR method to achieve isothermal, reaction-controlled conditions were 70 ± 10 μg and yielded residues of about 10 μg. Analytical capabilities were further limited by the need to remove the PP pyrolysis residues from the experimental sample plate with solvent. Removal of residues from the sample plates by mechanical means (i.e., scraping, tweezers, etc.) was found to be ineffective, with only use of excess 1,2,4-trichlorobenzene at 150°C consistently and reliably removing the residues. Consequently, the dissolved residues were dilute (~1 μg mL^{-1}) and not suitable for techniques like GPC, which require sample concentrations of ~1 mg mL^{-1}. An analysis of the product residue with ^{13}C solid-state NMR was made possible by combining multiple 250-μm-thick samples to meet the effective sample mass threshold of ~20 mg; however, commensurate with the results in Figure 5, these thick films were observed to have a low degree of conversion when pyrolyzed for 2.0 s because of the impact of transport limitations, and the NMR spectrum was unchanged compared with virgin PP. Additional details on the NMR analysis are provided alongside Figure S5.1.

A simple visual analysis of the formed residues was performed by examination with an optical microscope. Photographs of the samples reacted at 575°C for 20, 100, 220, and 500 ms taken through the eye piece of the microscope are shown in Figures 11C–11F. The sample reacted for 20 ms (Figure 11C) was primarily clear, with indications of bubbling because of gas and vapor product volatilization, and it retained its original circular shape and ~3.0-mm size. Similarly, the sample reacted for 100 ms (Figure 11D) mostly retained its original size and shape; however, the sample was notably darker, indicating potential formation of char-like material. The sample reacted for 220 ms (Figure 11E) had evidence of sample spreading and movement, as observed previously in the visual PHASR, as well as potential formation of char-like material. The sample reacted for 500 ms (Figure 11F) had a small amount of thin, dark residue, again indicative of potential formation of char-like material.

The product residues of samples reacted at 525°C for 20–2,000 ms as well as unreacted PP (including virgin PP, the original material prior to sample preparation, and a prepared thin film) were further analyzed by Raman, ATR-IR, and advanced ATR-IR-corrected spectroscopy. The notable results of these analyses are depicted

Table 2. Activation energies calculated from first principles with the Rice-Herzfeld model and from experimental PHASR data

Activation energy	Description	Value
$E_{a,R_1R_1}^{app}$	Rice-Herzfeld model calculated activation energy for R_1R_1 dominant termination	220 kJ mol^{-1}
$E_{a,R_2R_2}^{app}$	Rice-Herzfeld model calculated activation energy for R_2R_2 dominant termination	296 kJ mol^{-1}
$E_{a,R_1R_2}^{app}$	Rice-Herzfeld model calculated activation energy for R_1R_2 dominant termination	258 kJ mol^{-1}
$E_{a,GC}^{PHASR}$	PP pyrolysis experimental activation energy for production of light species up to C_{20} from PHASR intrinsic kinetic data	175 kJ mol^{-1}
$E_{a,MB}^{PHASR}$	overall experimental activation energy of PP pyrolysis from PHASR intrinsic kinetic data	242 kJ mol^{-1}

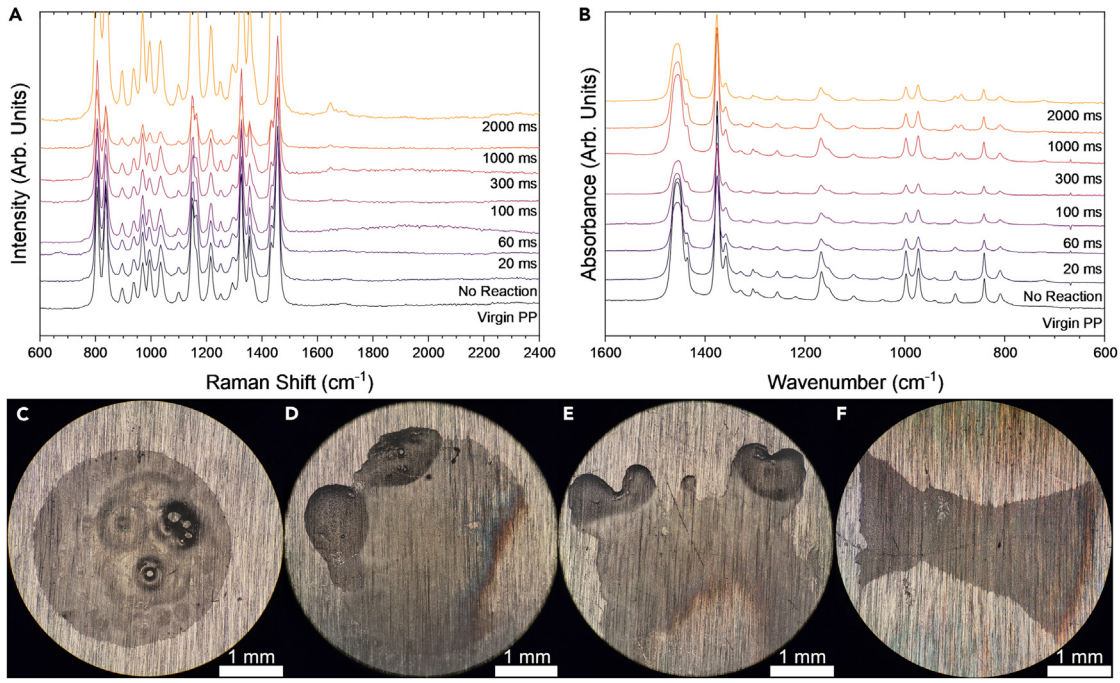

Figure 11. Analysis of solid residues

(A) Raman spectroscopy of polypropylene (PP) samples reacted at 525°C for 20–2,000 ms and comparison with unreacted PP (full spectra are provided in the supplemental information).

(B) Advanced attenuated total reflectance infrared (ATR-IR)-corrected spectroscopy of PP samples reacted at 525°C for 20–2,000 ms and comparison with unreacted PP (full spectra are provided in the supplemental information).

(C) Microscope photograph of a PP sample reacted for 20 ms at 575°C

(D) Microscope photograph of a PP sample reacted for 100 ms at 575°C

(E) Microscope photograph of a PP sample reacted for 220 ms at 575°C

(F) Microscope photograph of a PP sample reacted for 500 ms at 575°C.

in Figures 11A and 11B. In the Raman spectra (Figure 11A), a new peak was observed at ~1,648 cm^{-1} for samples reacted at 525°C for times equal to or greater than 100 ms that was not observed in unreacted and virgin PP samples. This peak corresponds to a substituted alkene C-C double bond.[109] In the advanced ATR-IR-corrected spectra (Figure 11B), a new peak was observed at ~886 cm^{-1} that was not present in the unreacted and virgin PP samples, which corresponds to a substituted alkene or aromatic C-H bonds.[109,110] The results from both analyses are indicative of the formation of unsaturated species that may be precursors to or polyaromatic in nature. The formation of these new chemical structures that react slower than virgin PP may explain the plateauing yields of volatile products in short reaction times up to 2.0 s, as depicted in Figure 9. Additional details on these analyses, including the full spectra, are available in Figures S5.2–S5.4.

Secondary PP pyrolysis kinetics

Spectroscopic analysis of the solid residues produced at short reaction times of up to 2.0 s in the PHASR reactor revealed the formation of unsaturated species. The stability of these residues was tested to determine whether these changes to the original PP prohibit further reaction or generate a secondary kinetic regime where the material pyrolyzes at a reduced rate at times beyond the measurement of the PHASR reactor. Under standard operation, the PHASR reaction is limited to reaction times of 2.0 s for a single pulse. This is an inherent safety limit of the PHASR power supply controller, which is designed to deliver high-current electrical pulses for times up to

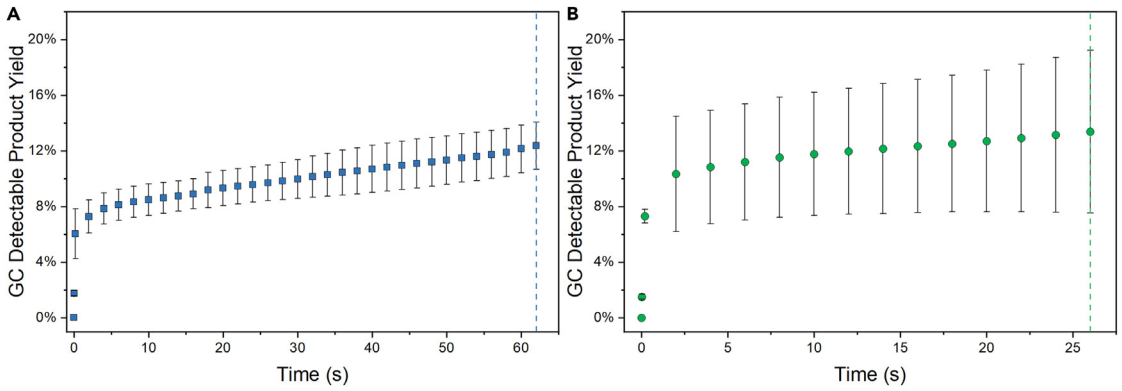

Figure 12. Secondary PP reaction kinetics

(A) Cumulative GC detected yields of PP samples pyrolyzed for 31 successive 2.0-s pulses (total reaction time of 62.0 s) at 500°C

(B) Cumulative GC detected yields of PP samples pyrolyzed for 13 successive 2.0-s pulses (total reaction time of 26.0 s) at 525°C.

The error bars represent the standard deviation of the data points.

2.0 s, that cannot be bypassed.[83] To probe reaction times longer than 2.0 s, we instead utilized multiple successive 2.0-s thermal pulses on individual samples.

When samples are reacted in the PHASR reactor, the sample plate undergoes intense stress induced by the high-current electrical pulses (~1.3 kA, 4 V) and rapid thermal swings (heating from room temperature up to 500°C–700°C in less than 20 ms and cooling back to room temperature in less than 180 ms). These extreme conditions lead to embrittlement of the sample plates, with some plates failing during a single pulse. For these long-reaction-time experiments, the vast majority of the sample plates failed after only two to four successive 2.0-s pulses (total reaction times of 4.0–8.0 s); however, three samples withstood 31 successive pulses at 500°C (total reaction time of 62.0 s), and two samples withstood 13 successive pulses at 525°C (total reaction time of 26.0 s). Lower reaction temperatures of 500°C and 525°C were chosen because they allow slightly lower amperage currents to be used, ~1.2 kA.

The average cumulative GC-detectable product yields from these samples are plotted in Figures 12A and 12B, with yield data from times shorter than 2.0 s from prior experiments also included. At 500°C (Figure 12A) and 525°C (Figure 12B), the GC-detectable yields achieved after 2.0 s were in agreement with the yield data in Figure 9, with average yields of ~7% and ~10%, respectively. In the multi-pulse experiments at 500°C and 525°C, the yields were observed to consistently rise with each thermal pulse after the initial 2.0 s up to ~12% and ~13%, respectively, after which the plates failed.

The reactivity of the solid residues at reaction times longer than 2.0 s was significantly slower than the fast, millisecond reactivity observed in the initial ~0.3 s of PP pyrolysis, revealing the existence of a secondary kinetic regime. This secondary kinetic regime likely results from desaturation of the original PP material, as detected by Raman and ATR-IR spectroscopy, as well as the presence of char-like material observed in the microscope photographs (Figure 11). PP pyrolysis at 525°C–625°C may be described by a two-stage lumped reaction system (Scheme 1). The first stage is characterized by rapid millisecond kinetics and the initial generation of gases and vapors, as well as solid pyrolysis residue. The second stage is characterized by the continued reaction of the solid residue to form additional gases and vapors as well as solid, unreactive char on the second-to-minute timescale. The kinetics of the secondary kinetic regime will be the focus of future work.

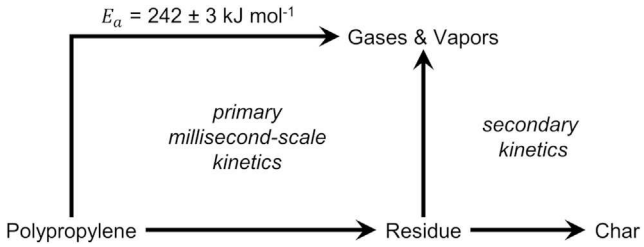

Scheme 1. Two-stage lumped reaction scheme for PP pyrolysis at 525°C–625°C
PP pyrolysis is described by a two-stage lumped reaction system characterized by rapid millisecond kinetics and initial generation of gases and vapors as well as solid pyrolysis residue (stage 1) and the continued reaction of the solid residue to form additional gases and vapors and solid, unreactive char on the second-to-minute timescale (stage 2).

Conclusions

The intrinsic reaction kinetics of PP pyrolysis were evaluated via the method of PHASR at temperatures spanning 525°C–625°C for reaction times between 20 ms and 2.0 s. The PHASR method was validated theoretically and experimentally to react ~15-μm thin films absent heat and mass transfer limitations. Direct observation of reacting PP films via high-speed photography elucidated reaction phenomena, including bubble formation, aerosol ejection, sample movement because of a potential Leidenfrost effect, and residue formation. A maximum plateau effect in the observed yields for reaction times less than 2.0 s was observed at all reaction conditions other than at 625°C, where complete reaction was reached in ~100 ms. A lumped first-order consumption model was used to determine the overall reaction kinetics, representative of the MB detectable yields, resulting in an activation energy of 242.0 ± 2.9 kJ mol^{-1} and a pre-exponential factor of 35.5 ± 0.6 ln(s^{-1}).The residues observed to form in the first 2.0 s of PP pyrolysis were shown to have a dark, char-like appearance, and formation of unsaturated species was detected by Raman and ATR-IR spectroscopy. The stability of residues was explored at reaction times exceeding 2.0 s, revealing the existence of a secondary kinetic regime in which the PP pyrolysis residue continues to react on the second-to-minute timescale. The kinetics of the slow, secondary kinetic regime will be the focus of future work.

EXPERIMENTAL PROCEDURES

Resource availability

Lead contact

Further information and requests for resources should be directed to and will be fulfilled by the lead contact, Dr. Paul J. Dauenhauer (hauer@umn.edu).

Materials availability

This study did not generate new unique reagents.

Data and code availability

The authors declare that all data supporting the findings of this study are available within the paper and its supplemental information file. Any additional information required to re-analyze the data reported in this paper is available from the lead contact upon request.

Reactor design

The PHASR reactor was originally developed for cellulose pyrolysis and has been redesigned to meet the challenges of polyolefin pyrolysis.[83,111] The redesigned PHASR reactor is capable of measuring the intrinsic kinetics of polyolefin pyrolysis

on the millisecond scale at temperatures up to 700°C. The primary features of the PHASR reactor redesign include a new cylindrical reactor housing, a flange seal with a copper O-ring, a modified heat exchanger, and beryllium copper contact brushes. As a result of these changes, the reactor body can be held at higher temperatures to prevent polyolefin pyrolysate condensation in the reactor. In addition, these changes result in faster, more consistent heating and cooling times ($\leq$20 ms and $\leq$180 ms, respectively) as well as more stable reaction temperatures. Full details of the reactor modifications and validation of reactor operating conditions are provided in previous work.[83]

A full description of the PHASR method has been provided previously,[83] and a summary of PHASR operation is presented here. To perform PHASR experiments, thin-film PP samples (15 μm thick, 3 mm in diameter) are deposited onto passivated carbon steel sample plates and placed into the reaction chamber. When the reactor is closed, electrical feedthroughs contact the sample plate via beryllium copper contact brushes, allowing a high-current electrical pulse to be delivered to the sample plate. This electrical pulse resistively heats the sample plate to the pre-selected reaction temperature ($\leq$ 700°C) for the set reaction time (20 ms–2.0 s); a cartoon depiction of reaction progress is shown in Figure 13E. During an electrical pulse, a 1,000-Hz optical pyrometer monitors the surface temperature of the sample and ensures precise temperature control through a PID feedback loop. Before performing a reaction, the reactor housing is heated to 300°C to prevent pyrolysate condensation. A silicon heat transfer fluid (Dow Syltherm 800) continuously flows through a gold-plated heat exchanger to rapidly cool the sample and quench the reaction. To prevent electrical shorting, an aluminum nitride ceramic sheet (0.010 in thick) is present between the sample plate and the heat exchanger. Helium continually sweeps the reaction chamber (~360 mL/min), providing an inert atmosphere and carrying all volatile products to an in-line gas chromatograph with a Polyarc and flame ionization detector (GC-PA-FID) for analysis. In this system, before analysis in the FID, all organic compounds are catalytically converted to methane in the PA, eliminating response factor changes because of different compounds and calibrations and improving analysis accuracy.[112]

Reactor operation

To operate under reaction-controlled conditions, thin-film samples were used in PHASR experiments. To prepare thin-film PP samples, PP pellets (provided by ExxonMobil Technology and Engineering, molecular weight [MW] ~263,000 g/mol by light scattering) were pressed in a Specac Mini-Film Maker at 175°C with 0.5 tons of force for 30 s. This produced thin-film discs (~1.5 cm in diameter) with thicknesses of 15–500 μm, from which individual 3.0-mm-diameter PP samples were cut using a Harris Uni-Core micro-punch. 15-μm-thick samples were primarily used for this work, and the thicknesses of the produced samples were verified using a KLA Tencor P-16 Surface Profiler, demonstrating that the average sample height is within ~1 μm of the desired 15-μm thickness (Figure 13B). Samples thinner than 15 μm were prepared by pressing the 15-μm samples again in the Mini-Film Maker (150°C, 1 ton force, 30 s), resulting in films with a thickness of ~6 μm and a diameter of ~4 mm (Table S2.1); example surface profilometry results are provided in Figure S2.1. For this work, initial sample weights were measured using a MB (Metter Toledo XPR2U). The samples were produced with a high level of control, as shown by the consistency of sample weight versus sample thickness (Figure 13C). After weighing, the samples were deposited onto carbon steel sample plates at 165°C until the samples slightly darkened on the surface (Figure 13A); this temperature was selected to prevent sample spreading during deposition. Prior to depositing the PP thin films, the sample plates were wiped with isopropanol and heated with a

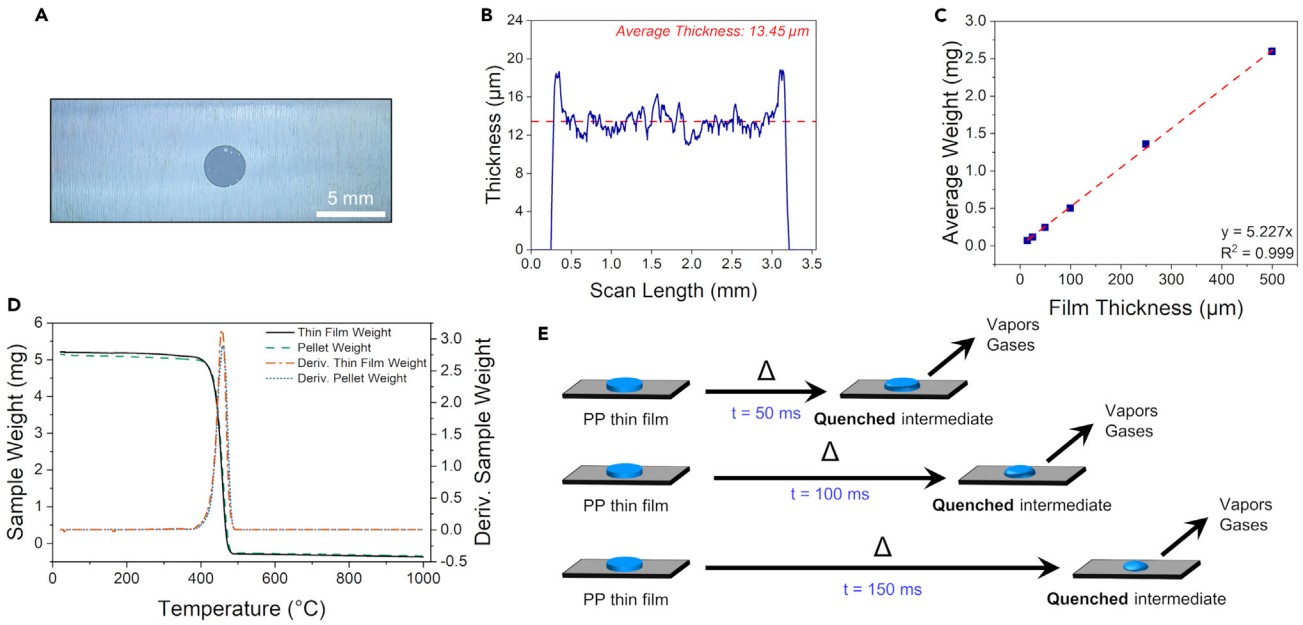

Figure 13. Thin-film PP samples

(A) Photograph of a 3-mm-diameter thin film deposited on a sample plate.

(B) Profilometry of a thin film showing an average thickness of ~13.5 µm.

(C) Uniformity of sample weights compared with sample thickness, as measured by MB.

(D) Consistency of a virgin PP pellet and PP thin-film TGA profiles, indicating no change of the thermal degradation properties of the sample.

(E) Cartoon depicting the reaction progress of a PP thin film.

butane torch until the metal turned blue, cleaning and passivating the surface. To ensure that the sample preparation process did not influence the degradation properties of PP, the original pellets and pressed thin-film samples of PP were pyrolyzed in a TGA (He atmosphere at 100 mL min^{-1}, 30°C to 1,000°C, 10 °C min^{-1} ramp rate). The weight loss and derivative curves for the original PP pellets and pressed PP thin films are overlaid in Figure 13D. The consistency between the original PP and the pressed PP indicates that no change to the degradation properties was caused by the sample preparation process.

In this work, samples were pyrolyzed over a range of temperatures (525°C, 550°C, 575°C, 600°C, and 625°C) for reaction times between 20 and 2,000 ms. The yield of light products (<C_{20}) was quantified via the in-line GC-PA-FID (GC-detectable yield). A deactivated fused silica column was utilized in the GC, resulting in a single light product peak. After pyrolysis, the amount of any remaining unreacted sample or residue on the plates was quantified with the XPR2U balance (MB). First, the excess area on the sample plates was cut off (to reduce the weight and improve weighing accuracy), and the plates were weighed. Then, the cut plates were soaked in 1,2,4-trichlorobenzene (TCB; 99%, Alfa Aesar) at 150°C for ~15 min to remove the remaining sample and residue. After drying in air, the clean plates were weighed again. The difference in the weights determined the weight of the remaining unreacted sample. Using the initial sample weights and the weight of remaining unreacted sample, the total yield of volatile products by mass was obtained (MB-detectable yield).

High-speed photography

A second, visual PHASR system was developed, which enables *in situ* observation of reacting PP pyrolysis samples via high-speed photography.[83] In this work, samples

were pyrolyzed over a range of temperatures (500°C, 550°C, 600°C, 650°C, and 700°C) for reaction times of 2,000 ms. In the visual PHASR reactor, samples were pyrolyzed in the same manner as with PHASR via controlled high-current electrical pulses. For this system, the top assembly of a PHASR reactor was inverted, and a 316 stainless steel riser containing clear polycarbonate side windows and a clear polycarbonate cover sealed the system, allowing a helium atmosphere as well as observation of the samples with the high-speed camera. The visual PHASR reactor is described in full detail in previous work.[83]

SUPPLEMENTAL INFORMATION

Supplemental information can be found online at https://doi.org/10.1016/j.matt.2023.07.020.

ACKNOWLEDGMENTS

We acknowledge financial support from the ExxonMobil Technology and Engineering Company and from the University of Minnesota Center for Sustainable Polymers under grant CHE-1901635. Parts of this work were carried out in the University of Minnesota Characterization Facility, which receives partial support from NSF through the MRSEC program. The Raman and ATR-IR spectroscopy used for residue characterization were conducted by and analyzed in consultation with Characterization Facility Senior Research Associate Dr. Bing Luo. Portions of this work were conducted in the Minnesota Nano Center, which is supported by the National Science Foundation through the National Nanotechnology Coordinated Infrastructure (NNCI) under award ECCS-2025124.

AUTHOR CONTRIBUTIONS

Conceptualization, N.S., I.M., and P.J.D.; methodology, N.S., I.M., and A.Z.; software, N.S., I.M., and Z.W.; formal analysis, N.S., Z.W., and M.N.; investigation, N.S.; resources, B.P., S.U., T.G., and S.M.; data curation, N.S.; writing – original draft, N.S.; writing – review & editing, all authors; visualization, N.S.; supervision, P.J.D., B.P., S.U., T.G., and S.M.; funding acquisition, P.J.D.

DECLARATION OF INTERESTS

The authors declare no competing interests.

Received: March 28, 2023
Revised: June 6, 2023
Accepted: July 19, 2023
Published: August 17, 2023

REFERENCES

1. Geyer, R. (2020). Production, use, and fate of synthetic polymers. In Plastic Waste and Recycling (Elsevier), pp. 13–32. https://doi.org/10.1016/B978-0-12-817880-5.00002-5.

2. Rabnawaz, M., Wyman, I., Auras, R., and Cheng, S. (2017). A roadmap towards green packaging: The current status and future outlook for polyesters in the packaging industry. Green Chem. *19*, 4737–4753. https://doi.org/10.1039/c7gc02521a.

3. Anuar Sharuddin, S.D., Abnisa, F., Wan Daud, W.M.A., and Aroua, M.K. (2016). A review on pyrolysis of plastic wastes. Energy Convers. Manag. *115*, 308–326. https://doi.org/10.1016/j.enconman.2016.02.037.

4. Gahleitner, M., and Paulik, C. (2017). Chapter 11 - Polypropylene and Other Polyolefins. In M. B. T.-B. P. M., E.E. Gilbert, ed. (Butterworth-Heinemann), pp. 279–309. https://doi.org/10.1016/B978-0-323-35824-8.00011-6.

5. Geyer, R., Jambeck, J.R., and Law, K.L. (2017). Production, use, and fate of all plastics ever made. Sci. Adv. *3*, e1700782. https://doi.org/10.1126/sciadv.1700782.

6. Payne, J., McKeown, P., and Jones, M.D. (2019). A circular economy approach to plastic waste. Polym. Degrad. Stabil. *165*, 170–181. https://doi.org/10.1016/j.polymdegradstab.2019.05.014.

7. Hopewell, J., Dvorak, R., and Kosior, E. (2009). Plastics recycling: challenges and opportunities. Philos. Trans. R. Soc. Lond. B Biol. Sci. *364*, 2115–2126. https://doi.org/10.1098/rstb.2008.0311.

8. Vollmer, I., Jenks, M.J.F., Roelands, M.C.P., White, R.J., van Harmelen, T., de Wild, P., van der Laan, G.P., Meirer, F., Keurentjes, J.T.F., and Weckhuysen, B.M. (2020). Beyond

Mechanical Recycling: Giving New Life to Plastic Waste. Angew Chem. Int. Ed. Engl. *59*, 15402–15423. https://doi.org/10.1002/anie.201915651.

9. Ragaert, K., Delva, L., and Van Geem, K. (2017). Mechanical and chemical recycling of solid plastic waste. Waste Manag. *69*, 24–58. https://doi.org/10.1016/j.wasman.2017.07.044.

10. Ignatyev, I.A., Thielemans, W., and Vander Beke, B. (2014). Recycling of Polymers: A Review. ChemSusChem *7*, 1579–1593. https://doi.org/10.1002/cssc.201300898.

11. Huysman, S., De Schaepmeester, J., Ragaert, K., Dewulf, J., and De Meester, S. (2017). Performance indicators for a circular economy: A case study on post-industrial plastic waste. Resour. Conserv. Recycl. *120*, 46–54. https://doi.org/10.1016/j.resconrec.2017.01.013.

12. Chen, X., Wang, Y., and Zhang, L. (2021). Recent Progress in the Chemical Upcycling of Plastic Wastes. ChemSusChem *14*, 4137–4151. https://doi.org/10.1002/cssc.202100868.

13. Lebedeva, E.A., Astaf'eva, S.A., Istomina, T.S., Trukhinov, D.K., Il'inykh, G.V., and Slyusar', N.N. (2020). Application of Low-Temperature Solvolysis for Processing of Reinforced Carbon Plastics. Russ. J. Appl. Chem. *93*, 845–853. https://doi.org/10.1134/S1070427220060117.

14. Ügdüler, S., Van Geem, K.M., Denolf, R., Roosen, M., Mys, N., Ragaert, K., and De Meester, S. (2020). Towards closed-loop recycling of multilayer and coloured PET plastic waste by alkaline hydrolysis. Green Chem. *22*, 5376–5394. https://doi.org/10.1039/d0gc00894j.

15. Kaminsky, W. (1995). Chemical recycling of mixed plastics of pyrolysis. Adv. Polym. Technol. *14*, 337–344. https://doi.org/10.1002/adv.1995.060140407.

16. Westerhout, R.W.J., Waanders, J., Kuipers, J.A.M., and van Swaaij, W.P.M. (1997). Kinetics of the Low-Temperature Pyrolysis of Polyethene, Polypropene, and Polystyrene Modeling, Experimental Determination, and Comparison with Literature Models and Data. Ind. Eng. Chem. Res. *36*, 1955–1964. https://doi.org/10.1021/ie960501m.

17. Buekens, A. (2006). Introduction to Feedstock Recycling of Plastics. In Feedstock Recycling and Pyrolysis of Waste Plastics, J. Scheirs and W. Kaminsky, eds. (John Wiley & Sons, Ltd), pp. 1–41. https://doi.org/10.1002/0470021543.ch1.

18. Aguado, J., Serrano, D.P., and Clark, J.H. (1999). Feedstock Recycling of Plastic Wastes (Royal Society of Chemistry). https://doi.org/10.1039/9781847550804.

19. Kiran, E., and Gillham, J.K. (1976). Pyrolysis-molecular weight chromatography: A new on-line system for analysis of polymers. II. Thermal decomposition of polyolefins: Polyethylene, polypropylene, polyisobutylene. J. Appl. Polym. Sci. *20*, 2045–2068. https://doi.org/10.1002/app.1976.070200803.

20. Kruse, T.M., Wong, H.-W., and Broadbelt, L.J. (2003). Mechanistic Modeling of Polymer Pyrolysis: Polypropylene. Macromolecules *36*, 9594–9607. https://doi.org/10.1021/ma030322y.

21. Knümann, R., and BOCKHORN, H. (1994). Investigation of the Kinetics of Pyrolysis of PVC by TG-MS-Analysis. Combust. Sci. Technol. *101*, 285–299. https://doi.org/10.1080/00102209408951877.

22. Chan, J.H., and Balke, S.T. (1997). The thermal degradation kinetics of polypropylene: Part I. Molecular weight distribution. Polym. Degrad. Stabil. *57*, 113–125. https://doi.org/10.1016/S0141-3910(96)00158-9.

23. Chan, J.H., and Balke, S.T. (1997). The thermal degradation kinetics of polypropylene: Part III. Thermogravimetric analyses. Polym. Degrad. Stabil. *57*, 135–149. https://doi.org/10.1016/S0141-3910(96)00160-7.

24. Bockhorn, H., Hornung, A., Hornung, U., and Schawaller, D. (1999). Kinetic study on the thermal degradation of polypropylene and polyethylene. J. Anal. Appl. Pyrolysis *48*, 93–109. https://doi.org/10.1016/S0165-2370(98)00131-4.

25. Gersten, J., Fainberg, V., Hetsroni, G., and Shindler, Y. (2000). Kinetic study of the thermal decomposition of polypropylene, oil shale, and their mixture. Fuel *79*, 1679–1686. https://doi.org/10.1016/S0016-2361(00)00002-8.

26. Yang, J., Miranda, R., and Roy, C. (2001). Using the DTG curve fitting method to determine the apparent kinetic parameters of thermal decomposition of polymers. Polym. Degrad. Stabil. *73*, 455–461. https://doi.org/10.1016/S0141-3910(01)00129-X.

27. Sørum, L., Grønli, M., and Hustad, J. (2001). Pyrolysis characteristics and kinetics of municipal solid wastes. Fuel *80*, 1217–1227. https://doi.org/10.1016/S0016-2361(00)00218-0.

28. Ballice, L., and Reimert, R. (2002). Classification of volatile products from the temperature-programmed pyrolysis of polypropylene (PP), atactic-polypropylene (APP) and thermogravimetrically derived kinetics of pyrolysis. Chem. Eng. Process *41*, 289–296. https://doi.org/10.1016/S0255-2701(01)00144-1.

29. Aguado, R., Olazar, M., Gaisán, B., Prieto, R., and Bilbao, J. (2002). Kinetic Study of Polyolefin Pyrolysis in a Conical Spouted Bed Reactor. Ind. Eng. Chem. Res. *41*, 4559–4566. https://doi.org/10.1021/ie0201260.

30. Moiseev, V.D., Neiman, M.B., and Kriukova, A.I. (1961). The thermal degradation of polypropylene. Polym. Sci. *2*, 55–62. https://doi.org/10.1016/0032-3950(61)90010-7.

31. Gao, Z., Kaneko, T., Amasaki, I., and Nakada, M. (2003). A kinetic study of thermal degradation of polypropylene. Polym. Degrad. Stabil. *80*, 269–274. https://doi.org/10.1016/S0141-3910(02)00407-X.

32. Kim, S.S., and Kim, S. (2004). Pyrolysis characteristics of polystyrene and polypropylene in a stirred batch reactor. Chem. Eng. J. *98*, 53–60. https://doi.org/10.1016/S1385-8947(03)00184-0.

33. Aboulkas, A., El Harfi, K., El Bouadili, A., Chanâa, M.B., and Mokhlisse, A. (2007). Pyrolysis kinetics of polypropylene. J. Therm. Anal. Calorim. *89*, 203–209. https://doi.org/10.1007/s10973-007-7398-z.

34. Encinar, J.M., and González, J. (2008). Pyrolysis of synthetic polymers and plastic wastes. Kinetic study. Fuel Process. Technol. *89*, 678–686. https://doi.org/10.1016/j.fuproc.2007.12.011.

35. Kim, S.B., Lee, W., Ryu, Y.W., Jung, J.-S., Song, J.-H., Lee, S.-W., and Kong, S.-H. (2008). Using isothermal kinetic results to estimate kinetic triplet of pyrolysis reaction of polypropylene. J. Microbiol. *46*, 100–107. https://doi.org/10.1016/j.jaap.2007.09.004.

36. Paik, P., and Kar, K.K. (2008). Kinetics of thermal degradation and estimation of lifetime for polypropylene particles: Effects of particle size. Polym. Degrad. Stabil. *93*, 24–35. https://doi.org/10.1016/J.POLYMDEGRADSTAB.2007.11.001.

37. Aboulkas, A., El Harfi, K., and El Bouadili, A. (2008). Non-isothermal kinetic studies on co-processing of olive residue and polypropylene. Energy Convers. Manag. *49*, 3666–3671. https://doi.org/10.1016/j.enconman.2008.06.029.

38. Aboulkas, A., El harfi, K., and El Bouadili, A. (2010). Thermal degradation behaviors of polyethylene and polypropylene. Part I: Pyrolysis kinetics and mechanisms. Energy Convers. Manag. *51*, 1363–1369. https://doi.org/10.1016/j.enconman.2009.12.017.

39. Fereidoon, A., Hemmati, M., Kordani, N., Kameli, M., Ghorbanzadeh Ahangari, M., and Sharifi, N. (2011). The Effect of Acid-Treatment of Carbon Nanotubes on the Thermal Kinetics of Isotactic Polypropylene. J. Macromol. Sci. Part B *50*, 665–678. https://doi.org/10.1080/00222341003784881.

40. Ali, M.F., Ahmed, S., and Qureshi, M.S. (2011). Catalytic coprocessing of coal and petroleum residues with waste plastics to produce transportation fuels. Fuel Process. Technol. *92*, 1109–1120. https://doi.org/10.1016/j.fuproc.2011.01.006.

41. Grassie, N., and Leeming, W.B.H. (1975). Some aspects of the photo, photothermal and thermal decomposition of polypropylene under vacuum. Eur. Polym. J. *11*, 809–818. https://doi.org/10.1016/0014-3057(75)90080-4.

42. Park, S.S., Seo, D.K., Lee, S.H., Yu, T.U., and Hwang, J. (2012). Study on pyrolysis characteristics of refuse plastic fuel using lab-scale tube furnace and thermogravimetric analysis reactor. J. Anal. Appl. Pyrolysis *97*, 29–38. https://doi.org/10.1016/j.jaap.2012.06.009.

43. Lecouvet, B., Bourbigot, S., Sclavons, M., and Bailly, C. (2012). Kinetics of the thermal and thermo-oxidative degradation of polypropylene/halloysite nanocomposites. Polym. Degrad. Stabil. *97*, 1745–1754. https://doi.org/10.1016/j.polymdegradstab.2012.06.022.

44. Suriapparao, D.V., Ojha, D.K., Ray, T., and Vinu, R. (2014). Kinetic analysis of co-pyrolysis of cellulose and polypropylene. J. Therm.

Anal. Calorim. *117*, 1441–1451. https://doi.org/10.1007/s10973-014-3866-4.

45. Wu, X., Wu, Y., Wu, K., Chen, Y., Hu, H., and Yang, M. (2015). Study on pyrolytic kinetics and behavior: The co-pyrolysis of microalgae and polypropylene. Bioresour. Technol. *192*, 522–528. https://doi.org/10.1016/j.biortech.2015.06.029.

46. Diaz Silvarrey, L.S., and Phan, A.N. (2016). Kinetic study of municipal plastic waste. Int. J. Hydrogen Energy *41*, 16352–16364. https://doi.org/10.1016/j.ijhydene.2016.05.202.

47. Das, P., and Tiwari, P. (2017). Thermal degradation kinetics of plastics and model selection. Thermochim. Acta *654*, 191–202. https://doi.org/10.1016/j.tca.2017.06.001.

48. Uzun, B.B., and Yaman, E. (2017). Pyrolysis kinetics of walnut shell and waste polyolefins using thermogravimetric analysis. J. Energy Inst. *90*, 825–837. https://doi.org/10.1016/j.joei.2016.09.001.

49. Nisar, J., Khan, M.A., Iqbal, M., Shah, A., Khan, R.A., Sayed, M., and Mahmood, T. (2018). Comparative Study of Kinetics of the Thermal Decomposition of Polypropylene Using Different Methods. Adv. Polym. Technol. *37*, 1168–1175. https://doi.org/10.1002/adv.21776.

50. Xu, F., Wang, B., Yang, D., Hao, J., Qiao, Y., and Tian, Y. (2018). Thermal degradation of typical plastics under high heating rate conditions by TG-FTIR: Pyrolysis behaviors and kinetic analysis. Energy Convers. Manag. *171*, 1106–1115. https://doi.org/10.1016/j.enconman.2018.06.047.

51. Burra, K.G., and Gupta, A.K. (2018). Kinetics of synergistic effects in co-pyrolysis of biomass with plastic wastes. Appl. Energy *220*, 408–418. https://doi.org/10.1016/j.apenergy.2018.03.117.

52. Murata, K., and Makino, T. (1975). Thermal Degradation of Polypropylene. Nippon Kagaku Kaishi *1975*, 192–200. https://doi.org/10.1246/nikkashi.1975.192.

53. Chen, R., Zhang, S., Cong, K., Li, Q., and Zhang, Y. (2020). Insight into synergistic effects of biomass-polypropylene co-pyrolysis using representative biomass constituents. Bioresour. Technol. *307*, 123243. https://doi.org/10.1016/j.biortech.2020.123243.

54. Lechleitner, A.E., Schubert, T., Hofer, W., and Lehner, M. (2020). Lumped kinetic modeling of polypropylene and polyethylene co-pyrolysis in tubular reactors. Processes *9*. 34–15. https://doi.org/10.3390/pr9010034.

55. Kulas, D.G., Zolghadr, A., and Shonnard, D. (2021). Micropyrolysis of Polyethylene and Polypropylene Prior to Bioconversion: The Effect of Reactor Temperature and Vapor Residence Time on Product Distribution. ACS Sustain. Chem. Eng. *9*, 14443–14450. https://doi.org/10.1021/acssuschemeng.1c04705.

56. Harmon, R.E., Sribala, G., Broadbelt, L.J., and Burnham, A.K. (2021). Insight into Polyethylene and Polypropylene Pyrolysis: Global and Mechanistic Models. Energy Fuels *35*, 6765–6775. https://doi.org/10.1021/acs.energyfuels.1c00342.

57. Pyo, S., Kim, Y.-M., Park, Y., Lee, S.B., Yoo, K.-S., Ali Khan, M., Jeon, B.-H., Jun Choi, Y., Hoon Rhee, G., and Park, Y.-K. (2021). Catalytic pyrolysis of polypropylene over Ga loaded HZSM-5. J. Ind. Eng. Chem. *103*, 136–141. https://doi.org/10.1016/j.jiec.2021.07.027.

58. Kim, Y.-M., Pyo, S., Hakimian, H., Yoo, K.-S., Rhee, G.-H., and Park, Y.-K. (2021). Kinetic Analysis for the Catalytic Pyrolysis of Polypropylene over Low Cost Mineral Catalysts. Sustainability *13*, 13386. https://doi.org/10.3390/su132313386.

59. Mitan, N.M.M., Yusuf, M.F., Brebu, M., Sari, M.M., and Hastuty, S. (2022). Study of pyrolysis kinetics on domestic plastic waste. AIP Conf. Proc. *2645*, 30006. https://doi.org/10.1063/5.0114067.

60. Nisar, J., Aziz, M., Shah, A., Shah, I., and Iqbal, M. (2022). Conversion of Polypropylene Waste into Value-Added Products: A Greener Approach. Molecules *27*, 3015. https://doi.org/10.3390/molecules27093015.

61. Zhang, Y., Fu, Z., Wang, W., Ji, G., Zhao, M., and Li, A. (2022). Kinetics, Product Evolution, and Mechanism for the Pyrolysis of Typical Plastic Waste. ACS Sustain. Chem. Eng. *10*, 91–103. https://doi.org/10.1021/acssuschemeng.1c04915.

62. Nisar, J., Khan, M.A., Ali, G., Iqbal, M., Din, M.I., Hussain, Z., Bhatti, I.A., Al-Kadhi, N.S., and Alamro, F.S. (2022). Polypropylene pyrolysis kinetics under isothermal and non-isothermal conditions: a comparative analysis. Zeitschrift fur Phys. Chemie *236*, 1163–1172. https://doi.org/10.1515/zpch-2022-0005.

63. Kiang, J.K.Y., Uden, P.C., and Chien, J.C.W. (1980). Polymer reactions—Part VII: Thermal pyrolysis of polypropylene. Polym. Degrad. Stabil. *2*, 113–127. https://doi.org/10.1016/0141-3910(80)90033-6.

64. Galiwango, E., and A Gabbar, H. (2022). Synergistic interactions, kinetic and thermodynamic analysis of co-pyrolysis of municipal paper and polypropylene waste. Waste Manag. *146*, 86–93. https://doi.org/10.1016/j.wasman.2022.04.032.

65. Dubdub, I. (2023). Kinetics Study of Polypropylene Pyrolysis by Non-Isothermal Thermogravimetric Analysis. Materials *16*, 584. https://doi.org/10.3390/ma16020584.

66. Sousa Pessoa De Amorim, M.T., Bouster, C., and Veron, J. (1982). Pyrolysis of polypropylene: II. Kinetics of degradation. J. Anal. Appl. Pyrolysis *4*, 103–115. https://doi.org/10.1016/0165-2370(82)80002-8.

67. Dickens, B. (1982). Thermal degradation study of isotactic polypropylene using factor-jump thermogravimetry. J. Polym. Sci. Polym. Chem. Ed. *20*, 1169–1183. https://doi.org/10.1002/pol.1982.170200502.

68. Gamboroža-Jukić, M., and Čunko, R. (1992). Kinetics of the thermal degradation of polypropylene fibres. Acta Polym. *43*, 258–260. https://doi.org/10.1002/actp.1992.010430503.

69. Wu, C.-H., Chang, C.-Y., Hor, J.-L., Shih, S.-M., Chen, L.-W., and Chang, F.-W. (1993). On the thermal treatment of plastic mixtures of MSW: Pyrolysis kinetics. Waste Manag. *13*, 221–235. https://doi.org/10.1016/0956-053X(93)90046-Y.

70. Jung, S.-H., Cho, M.-H., Kang, B.-S., and Kim, J.-S. (2010). Pyrolysis of a fraction of waste polypropylene and polyethylene for the recovery of BTX aromatics using a fluidized bed reactor. Fuel Process. Technol. *91*, 277–284. https://doi.org/10.1016/J.FUPROC.2009.10.009.

71. Mettler, M.S., Mushrif, S.H., Paulsen, A.D., Javadekar, A.D., Vlachos, D.G., and Dauenhauer, P.J. (2012). Revealing pyrolysis chemistry for biofuels production: Conversion of cellulose to furans and small oxygenates. Energy Environ. Sci. *5*, 5414–5424. https://doi.org/10.1039/C1EE02743C.

72. Maduskar, S., Facas, G.G., Papageorgiou, C., Williams, C.L., and Dauenhauer, P.J. (2018). Five Rules for Measuring Biomass Pyrolysis Rates: Pulse-Heated Analysis of Solid Reaction Kinetics of Lignocellulosic Biomass. ACS Sustain. Chem. Eng. *6*, 1387–1399. https://doi.org/10.1021/acssuschemeng.7b03785.

73. Bockhorn, H., Hornung, A., and Hornung, U. (1999). Mechanisms and kinetics of thermal decomposition of plastics from isothermal and dynamic measurements. J. Anal. Appl. Pyrolysis *50*, 77–101. https://doi.org/10.1016/S0165-2370(99)00026-1.

74. Proano-Aviles, J., Lindstrom, J.K., Johnston, P.A., and Brown, R.C. (2017). Heat and Mass Transfer Effects in a Furnace-Based Micropyrolyzer. Energy Technol. *5*, 189–195. https://doi.org/10.1002/ente.201600279.

75. Lédé, J. (2010). Biomass pyrolysis: Comments on some sources of confusions in the definitions of temperatures and heating rates. Energies *3*, 886–898. https://doi.org/10.3390/en3040886.

76. Hosaka, A., Watanabe, C., and Tsuge, S. (2007). Development of a new "flow-through" sample cup for the vertical micro-furnace pyrolyzer to reduce undesirable secondary reactions and band broadening of resulting pyrolyzates. J. Anal. Appl. Pyrolysis *78*, 452–455. https://doi.org/10.1016/j.jaap.2006.09.002.

77. Narayan, R., and Antal, M.J. (1996). Thermal Lag, Fusion, and the Compensation Effect during Biomass Pyrolysis. Ind. Eng. Chem. Res. *35*, 1711–1721. https://doi.org/10.1021/ie950368i.

78. Di Blasi, C. (1996). Kinetic and Heat Transfer Control in the Slow and Flash Pyrolysis of Solids. Ind. Eng. Chem. Res. *35*, 37–46. https://doi.org/10.1021/ie950243d.

79. Di Blasi, C., and Branca, C. (2003). Temperatures of wood particles in a hot sand bed fluidized by nitrogen. Energy Fuels *17*, 247–254. https://doi.org/10.1021/ef020146e.

80. Blasi, C.D. (2000). Modelling the fast pyrolysis of cellulosic particles in fluid-bed reactors. Chem. Eng. Sci. *55*, 5999–6013. https://doi.org/10.1016/S0009-2509(00)00406-1.

81. Völker, S., and Rieckmann, T. (2002). Thermokinetic investigation of cellulose pyrolysis - Impact of initial and final mass on kinetic results. J. Anal. Appl. Pyrolysis *62*,

165–177. https://doi.org/10.1016/S0165-2370(01)00113-9.

82. Authier, O., Ferrer, M., Mauviel, G., Khalfi, A.E., and Lédé, J. (2009). Wood fast pyrolysis: Comparison of Lagrangian and Eulerian modeling approaches with experimental measurements. Ind. Eng. Chem. Res. *48*, 4796–4809. https://doi.org/10.1021/ie801854c.

83. Zolghadr, A., Sidhu, N., Mastalski, I., Facas, G., Maduskar, S., Uppili, S., Go, T., Neurock, M., and Dauenhauer, P.J. (2021). On the Method of Pulse-Heated Analysis of Solid Reactions (PHASR) for Polyolefin Pyrolysis. ChemSusChem *14*, 4214–4227. https://doi.org/10.1002/cssc.202002667.

84. Wang, H., Chen, D., Yuan, G., Ma, X., and Dai, X. (2013). Morphological characteristics of waste polyethylene/polypropylene plastics during pyrolysis and representative morphological signal characterizing pyrolysis stages. Waste Manag. *33*, 327–339. https://doi.org/10.1016/j.wasman.2012.10.013.

85. Kim, S., and Kim, Y.-C. (2005). Using isothermal kinetic results to estimate the kinetic triplet of the pyrolysis of high density polyethylene. J. Anal. Appl. Pyrolysis *73*, 117–121. https://doi.org/10.1016/j.jaap.2005.01.001.

86. Teixeira, A.R., Gantt, R., Joseph, K.E., Maduskar, S., Paulsen, A.D., Krumm, C., Zhu, C., and Dauenhauer, P.J. (2016). Spontaneous Aerosol Ejection: Origin of Inorganic Particles in Biomass Pyrolysis. ChemSusChem *9*, 1322–1328. https://doi.org/10.1002/cssc.201600112.

87. Laidler, K.J., and Meiser, J.H. (1999). Physical Chemistry, 3rd ed. (Houghton Mifflin Company).

88. Barrie, P.J. (2012). The mathematical origins of the kinetic compensation effect: 1. the effect of random experimental errors. Phys. Chem. Chem. Phys. *14*, 318–326. https://doi.org/10.1039/c1cp22666e.

89. Barrie, P.J. (2012). The mathematical origins of the kinetic compensation effect: 2. the effect of systematic errors. Phys. Chem. Chem. Phys. *14*, 327–336. https://doi.org/10.1039/c1cp22667c.

90. Rice, F.O. (1931). THE THERMAL DECOMPOSITION OF ORGANIC COMPOUNDS FROM THE STANDPOINT OF FREE RADICALS. I. SATURATED HYDROCARBONS. J. Am. Chem. Soc. *53*, 1959–1972. https://doi.org/10.1021/ja01356a053.

91. Rice, F.O., Johnston, W.R., and Evering, B.L. (1932). THE THERMAL DECOMPOSITION OF ORGANIC COMPOUNDS FROM THE STANDPOINT OF FREE RADICALS. II. EXPERIMENTAL EVIDENCE OF THE DECOMPOSITION OF ORGANIC COMPOUNDS INTO FREE RADICALS. J. Am. Chem. Soc. *54*, 3529–3543. https://doi.org/10.1021/ja01348a007.

92. Rice, F.O. (1933). The Thermal Decomposition of Organic Compounds from the Standpoint of Free Radicals. III. The Calculation of the Products Formed from Paraffin Hydrocarbons. J. Am. Chem. Soc. *55*, 3035–3040. https://doi.org/10.1021/ja01334a075.

93. Rice, F.O., and Herzfeld, K.F. (1934). The Thermal Decomposition of Organic Compounds from the Standpoint of Free Radicals. VI. The Mechanism of Some Chain Reactions. J. Am. Chem. Soc. *56*, 284–289. https://doi.org/10.1021/ja01317a006.

94. Savage, P.E., and Klein, M.T. (1989). Kinetics of coupled reactions: Lumping pentadecylbenzene pyrolysis into three parallel chains. Chem. Eng. Sci. *44*, 985–991. https://doi.org/10.1016/0009-2509(89)85271-6.

95. Savage, P.E. (2000). Mechanisms and kinetics models for hydrocarbon pyrolysis. J. Anal. Appl. Pyrolysis *54*, 109–126. https://doi.org/10.1016/S0165-2370(99)00084-4.

96. Wang, Z. (2022). Methods and Mechanisms of Pyrolysis: Modeling Polymer Decomposition for a Circular Economy. Diss. Theses. (ProQuest).

97. Demirbas, A. (2004). Pyrolysis of municipal plastic wastes for recovery of gasoline-range hydrocarbons. J. Anal. Appl. Pyrolysis *72*, 97–102. https://doi.org/10.1016/j.jaap.2004.03.001.

98. Sogancioglu, M., Yel, E., and Ahmetli, G. (2020). Behaviour of waste polypropylene pyrolysis char-based epoxy composite materials. Environ. Sci. Pollut. Res. Int. *27*, 3871–3884. https://doi.org/10.1007/s11356-019-07028-3.

99. Liu, X., Burra, K.G., Wang, Z., Li, J., Che, D., and Gupta, A.K. (2020). On deconvolution for understanding synergistic effects in co-pyrolysis of pinewood and polypropylene. Appl. Energy *279*, 115811. https://doi.org/10.1016/j.apenergy.2020.115811.

100. Duan, D., Wang, Y., Dai, L., Ruan, R., Zhao, Y., Fan, L., Tayier, M., and Liu, Y. (2017). Ex-situ catalytic co-pyrolysis of lignin and polypropylene to upgrade bio-oil quality by microwave heating. Bioresour. Technol. *241*, 207–213. https://doi.org/10.1016/j.biortech.2017.04.104.

101. Abbas-Abadi, M.S., Haghighi, M.N., Yeganeh, H., and McDonald, A.G. (2014). Evaluation of pyrolysis process parameters on polypropylene degradation products. J. Anal. Appl. Pyrolysis *109*, 272–277. https://doi.org/10.1016/J.JAAP.2014.05.023.

102. Williams, E.A., and Williams, P.T. (1997). The pyrolysis of individual plastics and a plastic mixture in a fixed bed reactor. J. Chem. Technol. Biotechnol. *70*, 9–20. https://doi.org/10.1002/(SICI)1097-4660(199709)70:1<9::AID-JCTB700>3.0.CO;2-E.

103. Williams, E.A., and Williams, P.T. (1997). Analysis of products derived from the fast pyrolysis of plastic waste. J. Anal. Appl. Pyrolysis *40–41*, 347–363. https://doi.org/10.1016/S0165-2370(97)00048-X.

104. Donaj, P.J., Kaminsky, W., Buzeto, F., and Yang, W. (2012). Pyrolysis of polyolefins for increasing the yield of monomers' recovery. Waste Manag. *32*, 840–846. https://doi.org/10.1016/j.wasman.2011.10.009.

105. Shabtai, J., Xiao, X., and Zmierczak, W. (1997). Depolymerization-liquefaction of plastics and rubbers. 1. Polyethylene, polypropylene, and polybutadiene. Energy Fuels *11*, 76–87. https://doi.org/10.1021/ef960076+.

106. Ahmad, I., Khan, M.I., Khan, H., Ishaq, M., Tariq, R., Gul, K., and Ahmad, W. (2015). Pyrolysis Study of Polypropylene and Polyethylene Into Premium Oil Products. Int. J. Green Energy *12*, 663–671. https://doi.org/10.1080/15435075.2014.880146.

107. Harussani, M.M., Sapuan, S.M., Rashid, U., Khalina, A., and Ilyas, R.A. (2022). Pyrolysis of polypropylene plastic waste into carbonaceous char: Priority of plastic waste management amidst COVID-19 pandemic. Sci. Total Environ. *803*, 149911. https://doi.org/10.1016/j.scitotenv.2021.149911.

108. Sakata, Y., Uddin, M., and Muto, A. (1999). Degradation of polyethylene and polypropylene into fuel oil by using solid acid and non-acid catalysts. J. Anal. Appl. Pyrolysis *51*, 135–155. https://doi.org/10.1016/S0165-2370(99)00013-3.

109. Larkin, P.J. (2011). IR and Raman Spectroscopy: Principles and Spectral Interpretation (Elsevier).

110. Beauchamp P. Spectroscopy Tables. https://edisciplinas.usp.br/pluginfile.php/6971133/mod_resource/content/1/spec_ir_nmr_spectra_tables.pdf

111. Krumm, C., Pfaendtner, J., and Dauenhauer, P.J. (2016). Millisecond Pulsed Films Unify the Mechanisms of Cellulose Fragmentation. Chem. Mater. *28*, 3108–3114. https://doi.org/10.1021/acs.chemmater.6b00580.

112. Spanjers, C.S., Beach, C.A., Jones, A.J., and Dauenhauer, P.J. (2017). Increasing flame ionization detector (FID) sensitivity using post-column oxidation–methanation. Anal. Methods *9*, 1928–1934. https://doi.org/10.1039/C6AY03363F.